Mineralogical and geochemical constraints on magmatic evolution at Tengger Caldera, Indonesia

John Wardell

Thesis presented for the degree of Master of Research

Department of Earth and Planetary Sciences

Macquarie University

30th April 2018

Statement of Originality

I, John Wardell, declare the material presented in this thesis is my own original research except where otherwise acknowledged. This work has not previously been submitted for a degree or diploma in any university. To the best of my knowledge and belief, the thesis contains no material previously published or written by another person except where due reference is made in the thesis itself.

Signature: _____ Date: 30/04/2018

John Wardell

Abstract

A detailed mineralogical and geochemical study was carried out on stratigraphically well-constrained samples at Tengger Caldera Volcanic Complex (TCVC) to investigate the petrological and geochemical evolution of Tengger Caldera and the genetic relationship of the post-caldera volcanic cones to the pre-caldera magmatic system. The TCVC deposits are separated into the pre-caldera, caldera-forming and post-caldera eruptive episodes that span 820,000 years. These deposits range in composition from basalt, basaltic andesite to trachy-andesite and are tholeiitic to calc-alkaline in nature. The volcanic rocks define two geochemical groups based on major and trace element compositions: a low silica group and high silica group, with the initial caldera-forming eruption sequence characterised by low silica content. The post-caldera centres of Batok and Bromo show affinity to the low silica and high silica groups, respectively. Bromo rocks contain a more restricted range in plagioclase composition, towards lower An content compared to Batok. Bromo samples contain phenocrysts of pigeonite, which is absent elsewhere in the system. Thermobarometry estimates of crystallisation temperatures and pressures reveal two storage regions beneath the caldera: a shallow region at 7 to 11 km and a deeper region at 19 to 27 km. Magma feeding Bromo shows relativity deeper storage compared to that at Batok.

Acknowledgements

I would like friends and family for helping me get through the last 8 months in one piece and for any editing and multiple coffee provided to finish this thesis. A big thanks goes to my supervisors Heather Handley and Simon Turner for putting up with the many questions asked and for the help in planning out and execution of this thesis. I also want to thank Lucy McGee, Louise Goode, Shane Cronin and Rosa Didonna for the help in guiding me for parts of the study and brainstorming of ideas that help accomplished this thesis.

To Tim Murphy, Peter Wieland and Yi-Jen Lai at the Macquarie University GeoAnalytical Facility, thank you for the help in preparing and processing my samples and for solving the problems they caused. I would to further thank Tim Murphy for help and trouble shooting in regards to microprobe data and SEM work. I would also like to thank Scott Clark for the creation of the thin sections that were used in the thesis.

This research was supported by a Commonwealth Government funded Research Training Program Scholarship (RTP-MRES), The Department of Earth and Planetary Sciences at Macquarie University and an Australian Research Council Future Fellowship awarded to Heather Handley (FT120100440).

Contents

List of figures

Chapter 1

Chapter 2

Chapter 3

Chapter 4

List of tables

Chapter 2

Chapter 3

Chapter 4

Chapter 1: Introduction

Detailed petrological and geochemical studies of individual volcanoes and volcanic complexes are key to understanding their magmatic genesis and evolution. Previous stratigraphically-controlled geochemical studies of volcanic systems (e.g., Ruapehu, Gamble et al., 1999; Tatara-San Pedro, Dungan et al., 2001; Ambrym, Firth et al., 2016) suggest that differentiation processes in the crust control within-volcano geochemical variations rather than changes in source contributions. The composition-modifying differentiation processes commonly identified include fractional crystallisation, magma mixing and crustal contamination (Hildreth and Moorbath, 1988; Thirlwall et al., 1996; Tepley et al., 2000; Reubi and Nicholls, 2004; Davidson et al., 2005, Handley et al., 2007; 2010). Variations in volcanic rock geochemistry within individual systems may also be controlled by subvolcanic structure, which influence magma storage depths and ascent dynamics (e.g., Handley et al., 2007; Firth et al., 2016).

1.1 Tectonic setting of the Sunda arc and Java

Present day volcanism at the Sunda arc is driven by the subduction of the Australasian Plate beneath the Eurasian plate margin a rate of ~6-7 cm a year (Le Pichon, 1968; DeMets et al., 1990; Tregoning et al., 1994) (Fig. 1.1). The geology and tectonics of the Sunda arc subduction zone system is highly complex with along arc variations in the crustal structure consisting of varied compositions and age of the subducting slab and overlying sediments (Hamilton, 1979; Hall, 2011; Syracuse and Abers, 2006; Handley et al., 2014). The Sunda arc basement consists of a series of Gondwanan lithospheric fragments that were accreted during the Cretaceous to the Sundaland (pre-Cretaceous) margin (e.g., Metcalfe, 1990; Hall, 2011). The collision and subduction of the oceanic Roo Rise with the forearc has caused active erosion of the margin wedge and the retreat of the Java Trench between 109°E and 115°E (Kopp et al., 2006). This roughly corresponds across strike to the region of eastern Central Java and East Java (Fig. 1.1). Subduction of the Roo Rise has also produced a large variation in slab depth (vertical distance from the volcano to the subducting slab) along the Java sector of the arc with it increasing from Krakatau to Ungaran volcanoes before decreasing towards Ijen (Syracuse and Abers, 2006; Handley et al., 2014).

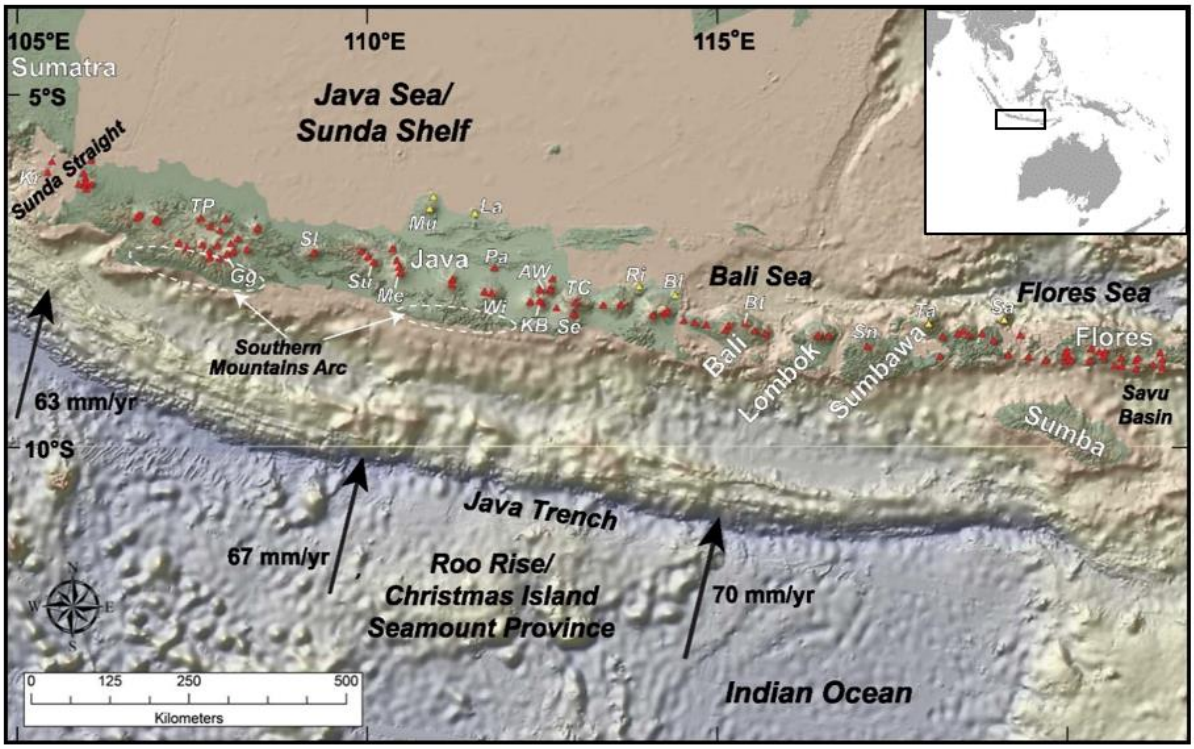

Figure 1.1: Relief of the central Sunda Arc produced from topographic (SRTM v.4) and bathymetric base datasets. Black arrows show convergence directions and rates of the Indo-Australian Plate and Sundaland. Triangles represent Quaternary volcanic structures with a basal diameter >3 km. Volcanoes Arjuno–Welirang (AW), Baluran (Bl), Batur (Bt), Galunggung (Gg), Kawi–Butak (KB), Krakatau (Kr), Lasem (La), Merapi (Me), Muriah (Mu), Papandan (Pa), Ringgit–Beser (Ri), SangeangApi (Sa), Sangenges (Sn), Semeru(Se), Slamet (Sl), Sumbing (Su), Tambora (Ta), Tankuban Prahu (TP), Tengger Caldera (TC) and Wilis (Wi). Modified from Pacey et al. (2013).

1.2 Geology of East Java

The Island of Java can be separated into four main Eocene-Miocene provinces overlying Mesozoic accretionary-collisional complexes (Smyth et al., 2005; Fig. 1.2). These provinces include the sedimentary and carbonate basins of the Kendeng and Rembang zones, the Southern Mountains Zone, an uplifted partly eroded volcanic arc, in addition to the present day Sunda volcanic arc (Smyth et al., 2005; 2008). These provinces are structurally controlled by a number of faults, with the primary faults being the Central Java Fault, the Kendeng thrust fault in East Java and Barabis, Cimandiri and Citandu faults in West Java (Simandjuntak and Barber, 1996). The active volcanic front in East Java is situated largely within the Kendeng basin, which consists of mainly volcanic-derived sedimentary material, particularly volcanic quartz, from the previously active Southern Mountains Arc to the south (Smyth et al., 2008; Clements et al., 2009; Fig. 1.2). Archean-Cambrian age zircons found within the Southern Mountains region indicate that it is underlain by a fragment of crust of Gondwanan origin that is not present further north, beneath the presently active volcanic front (Smyth et al., 2008).

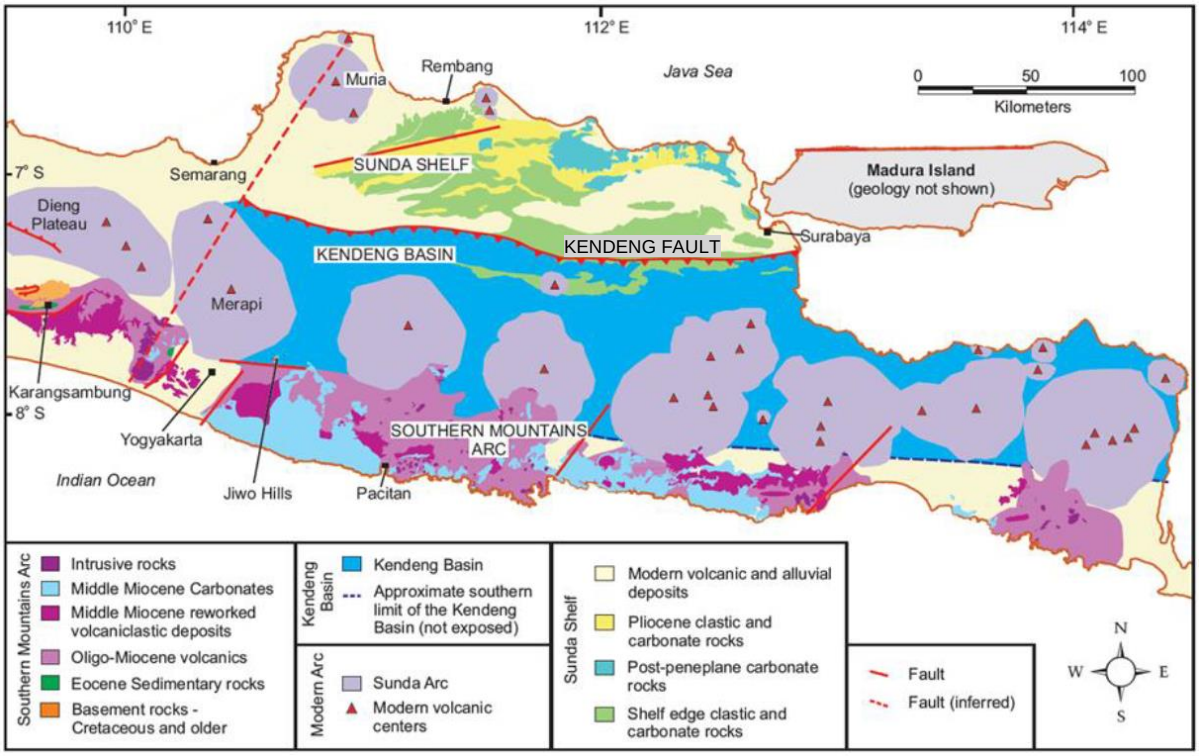

Figure 1.2. A simplified geological map of Eastern Java with geological provinces and stratigraphic units shown as well as prominent modern arc volcanoes and faults indicated. Taken from Smyth et al. (2008).

1.3 Geochemistry of Java

Quaternary volcanism in Java is dominantly calc-alkaline to high-K calc-alkaline in composition although tholeiitic and shoshonitic volcanic rocks have also been erupted (e.g., Katili, 1975; Whitford et al., 1979; Gertisser and Keller, 2003; Handley et al., 2007; 2008; 2010; 2014). Across arc changes in chemistry are widely recognised at the Sunda arc (e.g., Whitford and Nicholls, 1976; Hutchinson, 1976; Edwards, 1990) with the high-K alkaline volcanoes such as Muriah located the greatest distance above the subducting slab and across strike from the trench (Fig. 1.1). Along arc variations in Javanese volcano geochemistry and isotopic compositions were identified early on by Whitford (1975) who showed that the $^{87}Sr/^{86}Sr$ isotope ratios in calc-alkaline rocks increased over 500 km from Krakatau to the Dieng volcanic complex, then decreased eastwards to Bali. Since the 1970s there has been significant debate on the relative importance of source component versus shallow, crustal assimilation control on the observed spatial geochemical patterns (e.g., Whitford, 1975, 1982; Wheller et al., 1987; Gasparon and Varne, 1998; Turner and Foden, 2001; Gertisser and Keller, 2003a; Chadwick et al., 2007; Handley et al., 2007, 2011, 2014; Troll et al., 2013). A thorough assessment of the along-arc geochemical trends by Handley et al. (2014) suggests that despite a clear role for crustal assimilation at some centres in West and Central Java (e.g., Merapi),

heterogeneity in the subducted input (fluid and/or sediment melt) is needed to explain the significant geochemical and isotopic differences observed between West and East Java (e.g., Ba concentration, Ba/Hf ratio and Pb isotopic composition; Handley et al., 2014).

1.4 Tengger Caldera Volcanic Complex (TCVC)

Located in East Java, Tengger Caldera, also named the Sandsea Caldera, is one of three volcanic complexes within the Semeru-Tengger Massif (Mulyadi, 1992; Fig. 1.3). The Massif is made up of the TCVC (complete with the Tengger Caldera its intra-caldera cones of Mount Batok and Mount Bromo and the surrounding Sandsea), Ajek-Ajek and Jambangan calderas and Semeru (Solikhin et al., 2012; Fig. 1.3). Volcanism at the TCVC initiated around 820,000 years ago and consists of five overlapping stratovolcanoes, each truncated by a caldera (Smithsonian, 2017). In the surrounding region there are two older calderas (Fig. 1.3): one to the west of the TCVC and another to the north east that overlaps the eastern wall of Tengger Caldera, forming the Cemoro Lewang, which contains pyroclastic deposits up to 25 m thick (Froger et al., 1992). Tengger Caldera consists of two main units: a pre-caldera formation and post-caldera formation (Van Gerven and Pichler, 1995). The Pre-caldera formation consists of alternating pyroclastic flows and ash fall deposits in addition to thin lava flows that dip 10-25 degrees away from the caldera (Mulyadi, 1992).

The post-caldera formation comprises pyroclastic deposits from Mount Batok and the active Mount Bromo within the Tengger Caldera (Newhall and Dzurisin, 1989). The caldera also has four other post-caldera, intra-caldera volcanic centres (Fig. 1.3): the Segarawedi Kidul which was the first and largest centre to be generated, the Segarawedi Lor I and II craters which partially destroyed Segarawedi Kidul, and Mount Kursi (Van Gerven and Pichler, 1995; Fig. 1.3). Segarawdei Kidul was the only post-caldera, intra-caldera volcano to produce pyroclastic flow deposits with Segarawedi Lor and Kursi producing predominantly ash and lapilli fall deposits (Van Gerven and Pichler, 1995). Mount Batok and Bromo are the youngest in the group producing pyroclastic deposits, lava and ash fall deposits of ash mixed with lapilli (Mulyadi, 1992; Van Gerven and Pichler, 1995). Mount Batok is suggested to be the youngest post-caldera, intra-caldera volcano, forming a perfect scoria cone. However, activity shifted back to Bromo after the formation of Batok (Van Gerven and Pichler, 1995). Historic volcanic activity at Bromo is typically characterised by small, explosive phreatic eruptions with current discontinuous activity and degassing events ongoing since February 2016 (Smithsonian, 2017).

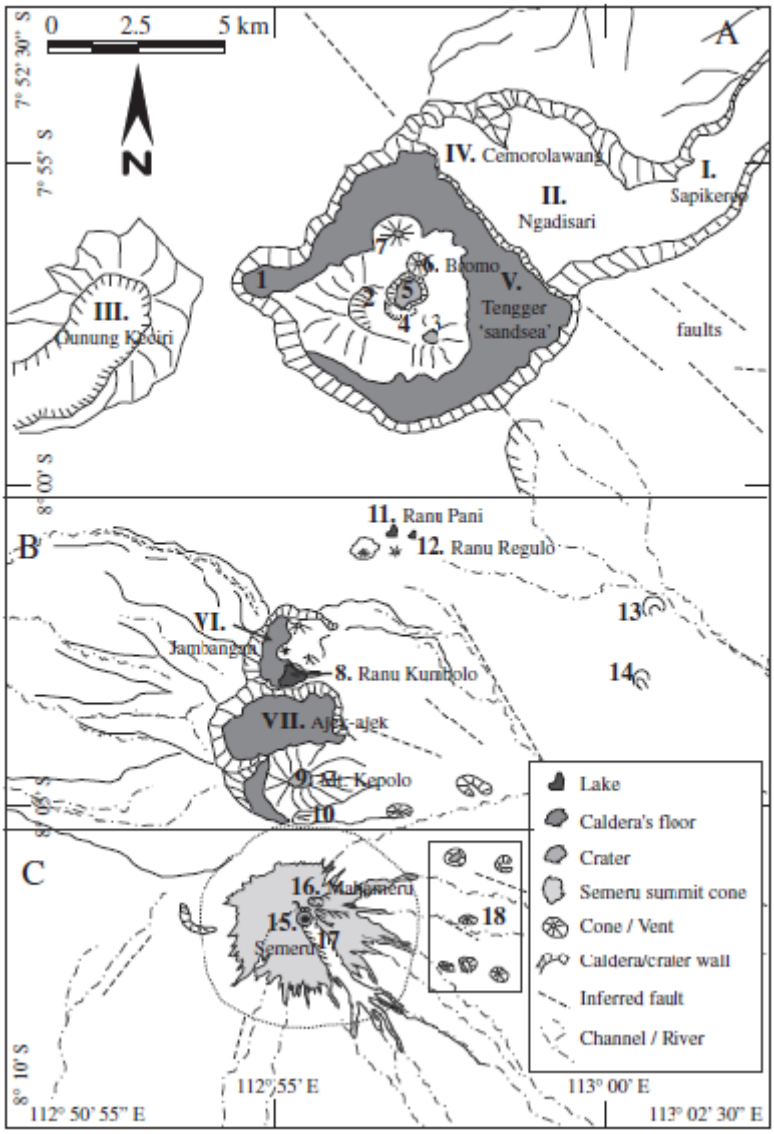

Figure 1.3: Sketch map showing the major landforms of the Semeru-Tengger Massif with; A) being the Tengger Caldera, B) being the Ajek-Ajek and Jambangan Caldera, and C) Semeru..Landforms indicated: I Sapikerep outlet valley; II the Ngadisari caldera; III Gunung Keciri; IV Cemorolawang caldera; and V Tengger 'sand-sea' (= ash-covered floor) caldera with Gunung Ijo (1), located in the west corner. The post-caldera volcanism has formed intracaldera cones inside the Tengger caldera: Gunung Widodaren (2), Gunung Kursi (3), Segarawedi Kidul (4), Segarawedi Lor (5), Gunung Bromo (6) and Gunung Batok (7). B. To the south lies Jambangan (VI) and Ajek-Ajek (VII) calderas. Several intra-caldera vents were formed including the maar of Ranu Kumbolo (8) in a deep crater. Mt. Kepolo strato-cone (9) is lined up with a youthful lava cone and flow (10). Ranu Pani (11) and Ranu Regulo (12) are maars, and two small vents (13 and 14) are located on the east flank. C. The youngest volcano in Semeru–Tengger massif, Semeru (15), including the currently active Jonggring-Seloko vent, inactive Mahameru (16) and Jambangan caldera to the north. The active vent sits at the top of the principal SE-trending scar (17) in the edifice. Several flank vents are visible on the eastern flanks (18). Taken from Solikhin et al. (2012)

There has been limited petrographic, mineralogical and geochemical research conducted on the TCVC in the last 20 years. Work in the 1990s by Mulyadi (1992; unpubished PhD thesis written

in French) and Van Gerven and Pichler (1995) produced major element and limited trace element data for samples from the caldera wall and the active Bromo intra-caldera cone. The medium- to high-K tholeiitic (transitional) andesites and basaltic andesites comprised plagioclase, orthopyroxene and clinopyroxene phenocrysts within a glassy and opaque mineral matrix. Magnetite, hematite and ilmenite ± chalcopyrite, the latter relating to a previous period of hydrothermal activity (Van Gerven and Pichler, 1995).

Other research on the TCVC has included geophysical and seismic analysis and gas sampling. Froger et al. (1992) conducted geophysical anomaly mapping of the TCVC and established that the complex was made up of multiple ancient calderas that were fed by two (now frozen) magma chambers to the west of Tengger in Nongkodjadjar Valley and the second being in the Wontoro Valley denoted by high gravity anomalies produced via Bouguer anomaly mapping. During the 1995 eruption of Bromo, seismic monitoring indicated that earthquake activity originated in the north-western section of Mount Bromo's crater (Gottschammer and Surono, 2000). More recently, Aiuppa et al. (2015) analysed magma-derived gas emissions during a degassing event during September 2014 and found that the gases emitted from Bromo were H_2O and SO_2 rich.

1.5 Thesis aims and structure

The main aims of this thesis are:

1. To use field observations and photographs along with the volcanic deposit characteristics (grain-size, texture, colour etc.) to develop an overall volcanic stratigraphy of the Tengger Caldera Volcanic Complex. This will enable the mineralogical and geochemical analysis of the deposits to be placed in a temporal and spatial context.

2. To evaluate mineralogical and geochemical (major and trace element) variations in volcanic rocks from the main eruptive phases and centres within the TCVC. These data will be used to investigate the petrological and geochemical evolution of the TCVC and the genetic relationship of the post-caldera volcanic cones to the pre-caldera magmatic system.

The thesis is comprised of a total of five chapters including this introductory chapter (Chapter 1). Chapter 2 presents the approach, methods and analytical techniques employed in this study.

Chapter 3 details the volcanology and stratigraphic context of the studied samples, the petrography, mineralogy and geochemical (major element contents and trace element concentrations) of TCVC rocks. Chapter 4 provides an estimation of the pre-eruptive temperatures and pressures (depths) of crystallisation prior to developing a petrogenetic model of magma dynamics (storage/evolution) at the TCVC, ascertain the genetic relationships of the different eruptive phases and vents. The geochemical variations from the TCVC are also compared to other Javanese volcanoes, and highlight contrasting differentiation trends compared with most other Javanese volcanoes. Chapter 5 summarises the research findings and suggests potential areas for future study.

Chapter 2: Approach and analytical methods

2.1 Sample selection and preparation

A total of 63 volcanic rock samples were collected from the Bromo-Tengger volcanic complex by Louise Goode in 2014. Sample localities are shown in Fig. 2.1., which consisted of samples located outside the caldera (T1-T14), the caldera wall (T16-T48 and T53-T63) and intra-caldera volcanic cones/centres (T15, T49-T52). Field observations and photographs were recorded at each locality. For this study, a subset of 27 samples was selected, comprising 20 tephra samples from deposits located throughout the complex and 7 volcanic bombs, lava and spatter blocks from inside the caldera (Fig. 2.1). Samples were chosen to capture the evolution of the volcanic complex, avoiding fine-grained tephra (ash) samples in order to minimise weathering or alteration.

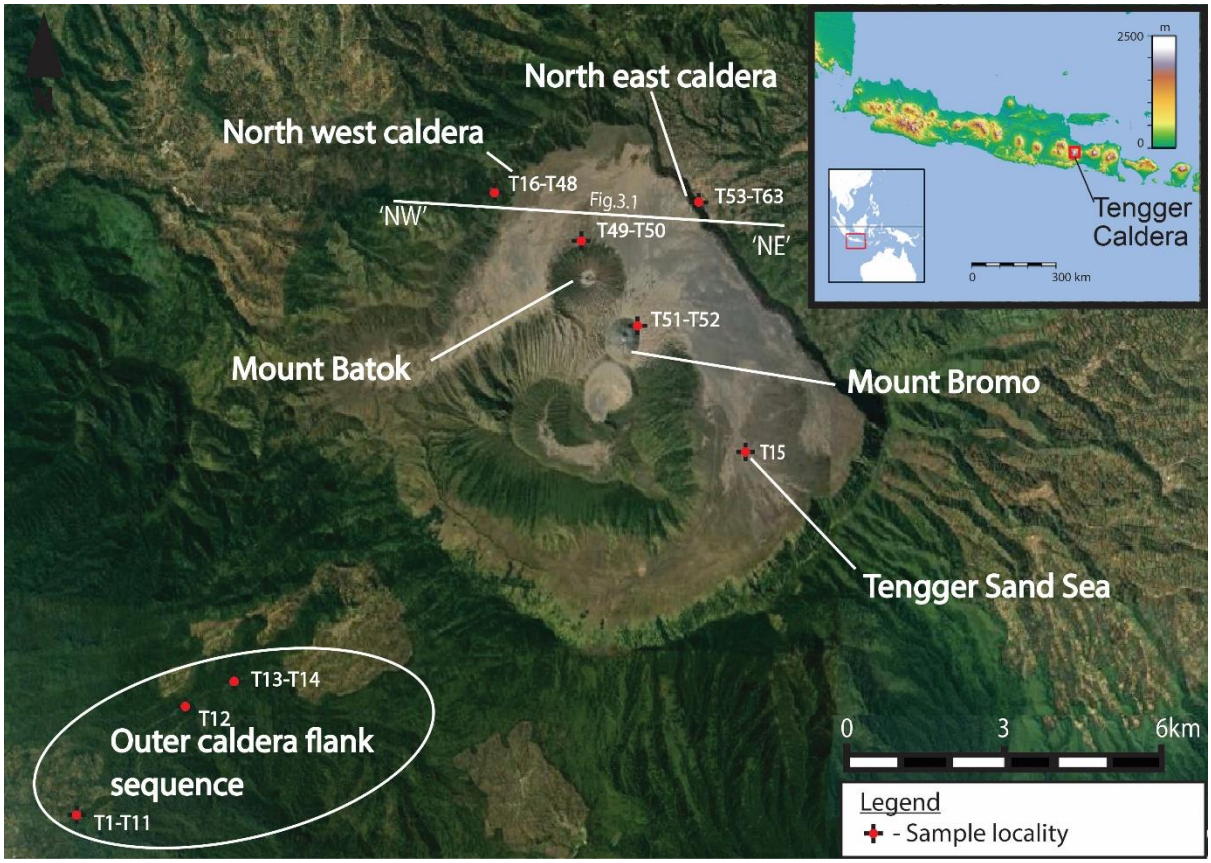

Figure 2.1: Satellite image of Tengger-Bromo Volcanic Complex with sample localities marked. Image modified from Google Earth (2017). Inset diagram shows the location of Tengger Caldera within East Java, Indonesia.

The 7 lava bombs, spatter and blocks were cut on a rock saw at Macquarie University to remove any weathered edges. A 28 x 48 mm block of the sample was made into a polished 100 µm-thick section by Thin Section Australia Pty Ltd. The remaining sample was then rinsed with Millipore deionised water and ultrasonicated for 30 minutes. Any remaining adhering material

was removed and the sample was rinsed again with Millipore deionised water before being dried in oven at 70°C overnight.

A cone and quartering technique was used to obtain two aliquots per tephra sample. The largest, juvenile lapilli were picked from one of the aliquots, which were then suspended in epoxy resin and polished into 100 µm-thick sections. For the second aliquot, the selected lapilli were washed with Millipore deionised water (between 2 and 7 times) and ultrasonicated in deionised water between 2 to 4 times to remove any adhered material. These samples were also dried in an oven at 70°C overnight.

2.2 Whole rock major analysis

For whole-rock major element analysis, glass discs were created via a fusion method and analysed by XRF at Macquarie University GeoAnalytical (MQGA). The tephra and lava samples were first crushed and milled into powder using a quartz aggregate mill and ring mil which were placed into plastic pre-cleaned (rinsed with deionised water and dried) containers. To determine total Loss on Ignition (LOI), empty ceramic crucibles were placed in the oven at 1100°C for 2 hours then weighed (n1). Then 1.5 g of a sample was placed into a crucible and weighed again (n2) before being placed into the furnace at 1100°C for a period of 24 hours to remove any possible water or volatiles from the samples. These were then removed and left to cool over a period of 15 to 20 minutes before placing in a desiccator. The samples were then weighed again to established the total mass (n3) and ascertain the Loss On Ignition (LOI) (weight %).

$$LOI\ (weight\ \%) = 100 \times \left(\frac{(n_2 - n_3)}{(n_2 - n_1)}\right)$$

For the glass discs, 1 g of sample and 10 g of flux (57% Lithium tetraborate to 43% Lithium metaborate) was measured into a platinum crucible before being placed into a furnace at 1100°C for 30 to 40 minutes to homogenise and fuse the sample using an automatic cradle. Once homogenisation between the flux and sample had been achieved, a platinum disc mould was placed into the furnace for 2 to 3 minutes and 1 ammonium iodide tablet was mixed with the flux-sample mixture. The crucible was then removed from the furnace and the flux-sample mixture was poured into the mould, which was left to cool for 5 minutes by fan forced cooling. The glass disc was then removed from the mould and cooled for 30 to 40 minutes. The disc was then placed in self-sealing polythene bag and stored in desiccator. The glass discs were

made in two batches, each containing external standards BHVO-2, BIR-1, BCR-2 and two internal standards T15 and T42. Samples were analysed using a Panalytical Axios 1kW XRF. Two independent analyses were completed for all 27 samples and standards as a means to cross check anomalous and data accuracy (Table 2.1).

Table 2.1: Comparison of major and trace element concentrations of the internal standard analysed (T42) and international rock standards measured in this study (compared to the accepted value).

	BIR-1			BCR-2			BHVO-2			Internal Standard (T42)			
	Accepted value	This study	DL	Accepted value	This study	DL	Accepted value	This study	DL	T42 (I)	T42 (II)	Average	1SD
Wt.%													
SiO_2	47.96	47.45	0.19	54	54.12	0.8	49.60	49.72	0.6	49.43	49.28	49.35	0.11
MgO	9.7	9.73	0.079	3.6	3.66	0.05	7.26	7.38	0.12	3.18	3.2	3.19	0.01
Na_2O	1.82	1.82	0.045	3.12	3.23	0.11	2.22	2.29	0.08	2.4	2.44	2.42	0.03
Al_2O_3	15.5	15.8	0.15	13.48	13.7	0.2	13.44	13.79	0.2	19.64	19.52	19.58	0.08
P_2O_5	0.02	0.02	0.001	0.359	0.38	0.02	0.269	0.27	0.02	0.25	0.25	0.25	0
TiO_2	0.96	0.94	0.01	2.27	2.24	0.05	2.73	2.71	0.04	1.35	1.35	1.35	0
CaO	13.3	13.38	0.12	7.11	7.17	0.11	11.40	11.49	0.2	8.38	8.37	8.38	0
K_2O	0.03	0	0.003	1.77	1.82	0.05	0.51	0.51	0.01	0.7	0.71	0.7	0.01
Fe_2O_3	2.06	11.46	0.1	13.77	13.87	0.2	12.39	12.51	0.2	11.39	11.36	11.38	0.02
MnO	0.175	0.18	0.003	0.197	0.2	0.06	0.169	0.17	0.04	0.2	0.2	0.2	0
ppm													
Sc	43.2	44.07	1	33.5	32.07	2	31.8	33.04	1	35.23	35.38	35.3	0.11
V	321	305.76	11	418	382.23	14	318	306.35	11	221.84	227.42	224.63	3.95
Cr	370	258.64	8	15.9	15.74	2	287	212.27	19	17.56	17.61	17.59	0.04
Co	52.2	51.79	2	37.3	34.83	3	44.9	43.81	3	33.26	33.36	33.31	0.07
Ni	169	173.72	6	12.6	12.65	1	120	124.55	7	18.53	18.82	18.67	0.2
Cu	121	126.95	4	19.7	25.36	2	129	143.51	7	187.38	192.11	189.75	3.35
Zn	70.4	65.24	9	130	121.18	9	104	101.18	6	102.98	103.56	103.27	0.41
Ga	15.5	15	1	22.1	20.71	2	21.4	20.67	0.9	22.23	22.53	22.38	0.22
Rb	0.21	0.2	1	46.0	45.81	2	9.26	9.26	1	23.47	24.38	23.93	0.64
Sr	108.6	109.53	2	337	328.66	14	394	387.27	23	470.33	480.82	475.58	7.41
Y	15.6	17.61	1	36.1	37.64	2	25.9	28.13	2	41.98	43.12	42.55	0.81
Zr	14.8	15.68	1	186.5	190.21	16	171.2	177.53	11	129.45	132.72	131.09	2.31
Nb	0.55	0.55	0.7	12.4	12.33	1	18.1	18.47	2	6.36	6.45	6.4	0.06
Mo	0.068	0.12	1	250.6	245.88	17	4.07	3.56	1	0.74	0.75	0.75	0
Cd	0.077	0.08	1	0.69	0.37	1	0.152	0.09	1	0.17	0.18	0.18	0
Cs	0.0065	0.01	1	1.16	1.17	0.1	0.100	0.11	1	1.92	2	1.96	0.06
Ba	6.75	6.62	1	684	651.2	28	130.9	131.28	13	697.95	739.68	718.82	29.5
La	0.564	0.63	0.07	25.08	24.43	1	15.2	15.16	1	15.22	16.11	15.67	0.63
Ce	1.92	1.94	0.4	53.1	51.1	2	37.2	37.12	2	36.42	38.39	37.4	1.39
Pr	0.372	0.39	1	6.83	6.63	0.3	5.29	5.4	1	4.88	5.07	4.97	0.14
Nd	2.30	2.42	0.7	28.3	27.65	2	23.8	24.28	1.8	21.97	22.74	22.35	0.55
Sm	1.113	1.14	1	6.55	6.38	0.3	6.14	6.15	0.4	5.83	6.02	5.93	0.13
Eu	0.520	0.5	0.05	1.99	1.97	0.1	2.04	1.97	1	1.86	1.92	1.89	0.05
Tb	0.362	0.37	1	1.055	1.04	0.04	0.939	0.95	1	1.08	1.1	1.09	0.02
Gd	1.90	1.92	0.4	6.67	6.63	0.3	6.21	6.32	0.2	6.75	6.88	6.81	0.09
Dy	2.54	2.6	1	6.42	6.09	1	5.28	5.24	1	6.64	6.78	6.71	0.1
Ho	0.572	0.61	1	1.313	1.29	0.06	0.989	1.01	0.04	1.44	1.47	1.45	0.02
Er	1.68	1.75	1	3.63	3.6	1	2.49	2.56	1	4.04	4.17	4.11	0.09
Yb	1.65	1.66	0.1	3.39	3.22	0.2	1.95	1.98	0.2	3.72	3.79	3.75	0.05
Lu	0.248	0.25	1	0.505	0.47	0.02	0.275	0.28	0.01	0.57	0.57	0.57	0
Hf	0.58	0.58	0.08	4.97	4.58	0.2	4.47	4.33	0.3	3.39	3.41	3.4	0.01
Ta	0.041	0.04	1	0.79	0.72	1	1.15	1.13	1	0.37	0.38	0.38	0
Th	0.033	0.03	1	5.83	5.88	0.7	1.22	1.25	0.3	3.18	3.21	3.2	0.02
U	0.011	0.01	1	1.68	1.6	0.19	0.41	0.42	1	0.74	0.74	0.74	0

Major element data analysed via XRF; Trace element data analysed via ICP-MS. DL= Detection limit; 1SD= One standard deviation. BIR-1, BCR-2 and BHVO-2 recorded values and detection limits are obtained from USGS datasheet of the respective samples.

2.3 Whole rock trace element analysis

Whole rock digestions for solution inductively coupled plasma mass spectrometry (ICP-MS) were prepared using the following method: 0.1g of sample powder was weighed out to 4 decimal places into clean 15ml Savillex® Teflon beakers. 2ml of concentrated HF (Merck Suprapur) and HNO3 (Teflon distilled Merck Analar) were added in a 1:1 ratio and refluxed overnight at 150oC. The solution was dried down, and this step repeated. 1ml of HF and 10 drops of perchloric acid (Merck Suprapur) were added and refluxed at 170°C overnight. The solution was then sequentially dried at 150°C, 170°C and 190°C. 2ml of 6N HCl (Teflon distilled Merck Analar) was added, and this was refluxed overnight then dried down. 2ml of 6N HNO3 was added and refluxed overnight before drying down to a gel-like texture.

In the final step, the sample was brought back into solution in 2% HNO3 + trace HF and further diluted to 100ml. Each diluted sample was then spiked with a mixture of ^{6}Li, As, Rh, In and Bi to correct for instrumental drift. Analysis was undertaken on an Agilent quadrupole ICP-MS 7500cs at Macquarie University GeoAnalytical (MQGA). BCR-2 was used as the calibration standard using concentrations reported via Geological and Environmental reference materials (GeoReM) by Jochum Klaus et al. (2007). The USGS standards BIR-1 and BHVO-2 were processed with the samples, diluted 1/1000, 1/2000 and 1/5000 times and analysed as unknowns to check the validity of the method. A method blank was processed to assess the cleanliness of the reagents used and was found to be negligible. All standard data are presented in Table 2.1.

2.4 Mineral analysis

Selected polished, thick sections were imaged by a petrographical microscope and stitched together using a NIS-element viewer via a NIKON camera attachment to produce 2x objective images of the complete section.

Elemental mapping, further sample imaging and mineral identification was conducted using an M4 Tornado XRF machine at MQGA. The M4 Tornado (micro-XRF) was used to scan the selected regions of the thin sections using a 20 µm spot size and X-ray beam of 50 keV and 600 µA under a vacuum of 20 mbar.

Mineral analysis was conducted on carbon-coated polished thick sections using a Cameca SX-100 electron microprobe at MQGA using a beam current of 20 nA and an accelerated voltage of 15 kV and a beam width of 1 µm. Major elements Si, Al, Mg, Fe, Ti, Ca, K, Na, Cr, Ni, Mn and P were analysed using a silicate mineral setup for the spectrometers. Analysis run time for each analysis point was 4 minutes with the detection limits for Al, Mg, K, Ca, Ti are 0.01 or lower, Na, Si, Cr, Ni are around 0.03, while Fe is slightly higher at 0.05. Images of minerals from the carbon coated thin sections were taken using a Zeiss EVO MA15 Scanning Electron Microprobe (SEM) using a voltage of 15 kV.

Chapter 3: Results

3.1 Volcanology

Fieldwork within the Sandsea caldera of the TCVC was carried out in 2014 by Louise Goode and Shane Cronin. Samples were collected from seven localities including extra-caldera deposits on the flank of the caldera, the north west caldera wall, north east caldera wall and post-caldera volcanic centres. The majority of samples investigated in this study were collected from the north west caldera wall (Table 3.1). The north west caldera wall is predominately made up of alternating tephra deposits, ignimbrite and lavas relating to pre-caldera, caldera-forming and post-caldera volcanic activity. A similar stratigraphy for the caldera wall was described by Van Gerven and Pichler (1995). The major stratigraphic units are detailed in Fig. 3.1 and stratigraphic sections of a 60 m section of the north west caldera wall, 5 m section of the north east wall and 7 m section of the outer flank parasitic cone sequence are presented in Fig. 3.2.

Table 1. Tengger Caldera Complex sample location, rock type and deposit details.

Sample#	Latitude	Longitude	Sample type	Event	Deposit
T1	8° 0' 36.8143" S	112° 51' 41.9353" E	Tephra fall	Outer caldera flank	Scoriaceous and fine lapilli at base.
T4	8° 0' 36.8143" S	112° 51' 41.9353" E	Tephra fall	Outer caldera flank	Coarse lapilli.
T5	8° 0' 36.8143" S	112° 51' 41.9353" E	Tephra fall	Outer caldera flank	Fine-medium lapilli unit, separated by ash layer.
T6	8° 0' 36.8143" S	112° 51' 41.9353" E	Tephra fall	Outer caldera flank	Fine-med lapilli bi-part layer.
T12	7° 59' 38.9584" S	112° 52' 50.8271" E	Tephra fall	Outer caldera flank	Massive unit of scoriaceous coarse lapilli.
T14	7° 59' 26.318" S	112° 53' 22.0157" E	Tephra fall	Outer caldera flank	Med-coarse lapilli with overlying weathered soil.
T15	7° 57' 30.7501" S	112° 58' 21.4446" E	Lava	Intra-caldera	Lava within Sandsea area (Tengger Caldera floor).
T24	7° 55' 22.6481" S	112° 55' 56.3196" E	Tephra fall	Post caldera	Fine-med lapilli unit below soil unit.
T25	7° 55' 22.6481" S	112° 55' 56.3196" E	Tephra fall	Post caldera	Coarse med lapilli unit.
T31	7° 55' 22.6481" S	112° 55' 56.3196" E	Tephra fall	Post caldera	Fine-med lapilli.
T32	7° 55' 22.6481" S	112° 55' 56.3196" E	Tephra fall	Caldera forming (2)	Coarse lapilli unit.
T35	7° 55' 22.6481" S	112° 55' 56.3196" E	Tephra fall	Caldera forming (2)	Fine-med lapilli unit with successions lapilli and surge ash with soil.
T36	7° 55' 22.6481" S	112° 55' 56.3196" E	Tephra fall	Caldera forming (2)	Massive scoria unit bedded medium lapilli unit.
T37	7° 55' 22.6481" S	112° 55' 56.3196" E	Tephra fall	Caldera forming (2)	Bedded coarse lapilli and scoria
T38	7° 55' 22.6481" S	112° 55' 56.3196" E	Tephra fall	Caldera forming (2)	Massive med-coarse lapilli fall unit.
T39	7° 55' 22.6481" S	112° 55' 56.3196" E	Tephra fall	Caldera forming (2)	Fine-med lapilli interbedded fine ash layer.
T40	7° 55' 22.6481" S	112° 55' 56.3196" E	Bomb	Caldera forming (2)	Massive bomb in tephra fall
T42	7° 55' 22.6481" S	112° 55' 56.3196" E	Tephra fall	Caldera forming (1)	Fine lapilli unit.
T43	7° 55' 22.6481" S	112° 55' 56.3196" E	Lava Spatter	Caldera forming (1)	Lava spatter in med-fine lapilli unit.
T44	7° 55' 22.6481" S	112° 55' 56.3196" E	Ignimbrite	Caldera forming (1)	Welded lava spatter
T45	7° 55' 22.6481" S	112° 55' 56.3196" E	Tephra fall	Caldera forming (1)	Bedded scoraceious units and pumaceious lapilli layers with fine ash imbedded.
T46	7° 55' 22.6481" S	112° 55' 56.3196" E	Tephra fall	Caldera forming (1)	Fine pumice rich layer.

T47	7° 55' 22.6481" S	112° 55' 56.3196" E	Ignimbrite	Caldera forming (1)	Bomb of lava spatter in welded ignimbrite
T48	7° 55' 22.6481" S	112° 55' 56.3196" E	Lava	Pre-caldera	Lava flow at base of caldera wall
T49	7° 55' 45.588" S	112° 56' 46.3402" E	Lava	Intra-caldera	Mt. Batok cinder cone lava
T50	7° 55' 45.588" S	112° 56' 46.3402" E	Lava	Intra-caldera	Mt. Batok cinder cone lava
T51	7° 56' 28.0043" S	112° 57' 19.0868" E	Tephra fall	Intra-caldera	Tephra from Mt. Bromo crater
T52a	7° 56' 28.0043" S	112° 57' 19.0868" E	Lava Spatter	Intra-caldera	Bomb from Mt. Bromo crater
T52b	7° 56' 28.0043" S	112° 57' 19.0868" E	Lava Spatter	Intra-caldera	Bomb from Mt. Bromo crater
T55	7° 55' 26.656" S	112° 57' 53.595" E	Tephra fall	Caldera forming (2)	Medium lapilli and pumice rich unit.
T59	7° 55' 26.656" S	112° 57' 53.595" E	Tephra fall	Caldera forming (2)	Coarse lapilli unit.
T63	7° 55' 26.656" S	112° 57' 53.595" E	Ignimbrite	Caldera forming (1)	Lava spatter at base

Highlighted samples were selected for whole-rock trace element geochemical analysis.

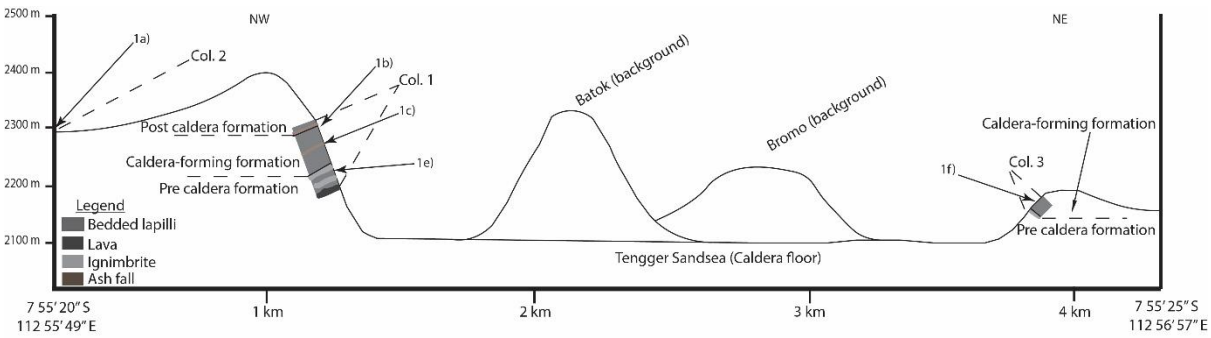

Figure 3.1. Topographic cross section of Tengger Caldera and associated intra-caldera cones showing the location of the stratigraphic columns and generalised geology of the north west and north east caldera walls. Annotated parts of each section relate to photographs from Figure 3.3.

3.1.1 Pre-caldera and Caldera-forming (1) sequences

The Pre-caldera sequence constitutes the lowest section of the north western caldera wall and is dominated by large blocky lava flows of basaltic andesite and ignimbrite (Fig. 3.2: Col. 1). Above the pre-caldera sequence lies the first caldera-forming sequence (Caldera-forming 1), which overlies the pre-caldera lavas with 2 to 3 m-thick fine ash to medium lapilli beds with interbedded ash fall. This layer is covered by massive blocky ignimbrite composed of lava spatter and welded tephra (T47) (Fig. 3.3e). The ignimbrite is overlain by poorly-sorted alternating beds of medium to coarse lapilli and fine ash layers which is capped by another ignimbrite layer consisting of lava spatter, pumice and large blocks of lava (T44). This ignimbrite deposit is similarly seen on the north eastern wall producing lava spatter (T63) at the base of stratigraphy (Fig. 3.2. Col. 3). This sequence is terminated above the ignimbrite by a sharp transition into bedded large ash and lapilli with intercalated lava spatter and bombs (T42 and T43) (Fig. 3.2. Col. 1).

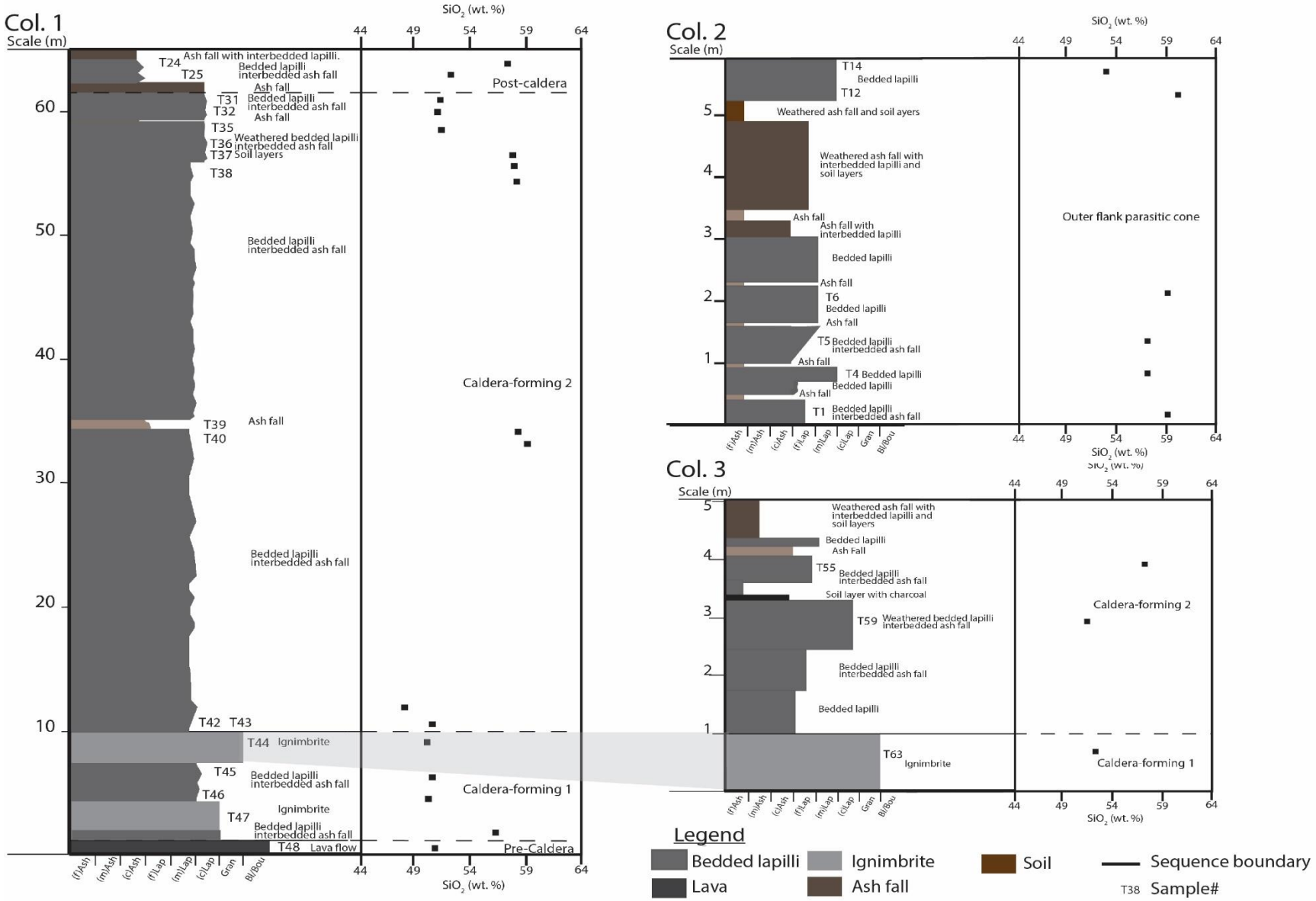

Figure 3.2: The stratigraphy and whole rock SiO_2 content from different localities within the TCVC. Col 1.) The north west caldera wall; Col 2.) North Eastern caldera wall. Col. 3) The outer caldera flank sequence. SiO_2 relates to the respective sample in the stratigraphy.

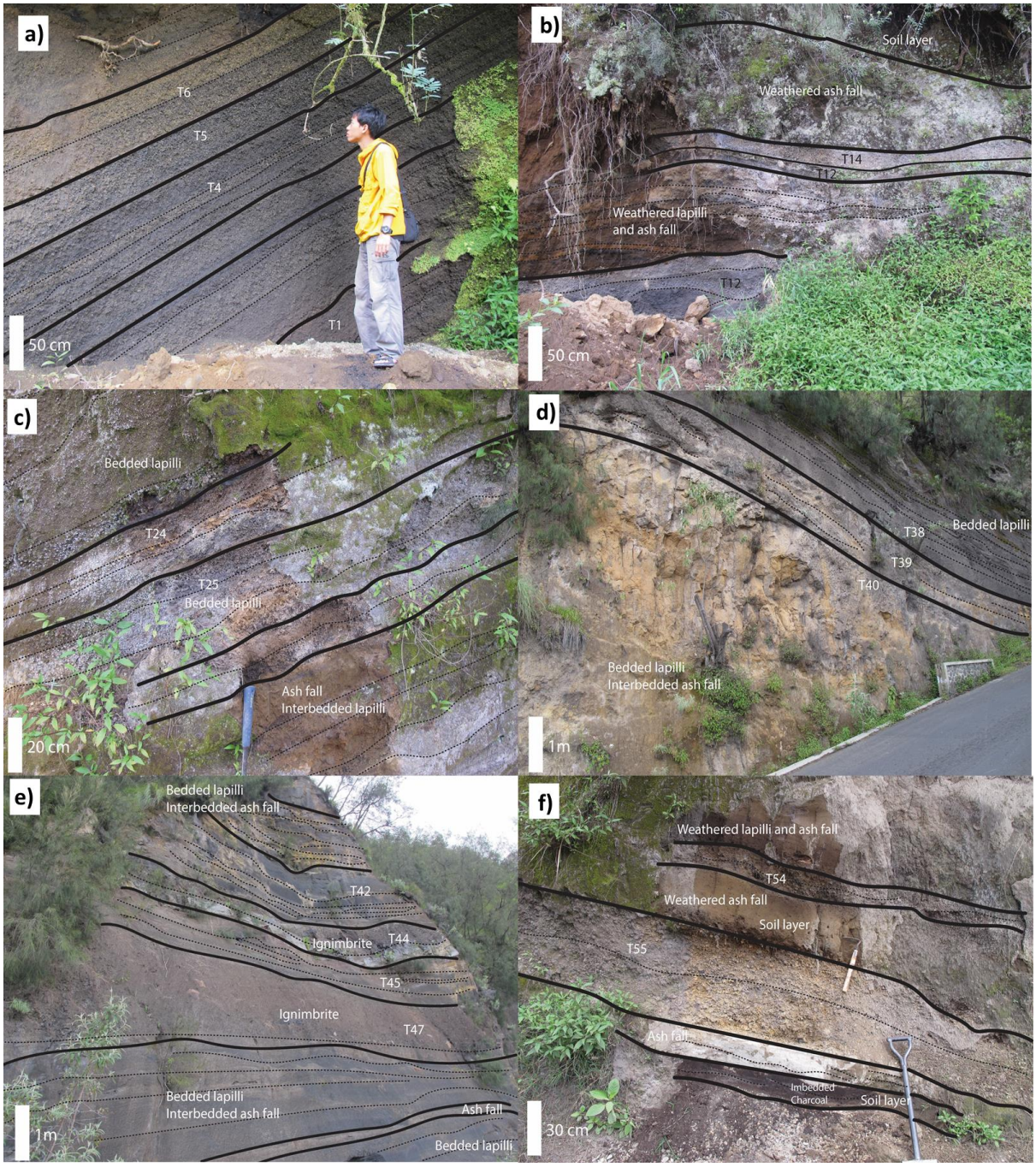

Figure 3.3. Field photographs showing: a) the outer flank (parasitic sequence) deposits (outside of the Tengger caldera); b) the upper tephra deposits of the outer flank sequence; c) the post caldera sequence of the north west caldera wall; d) the caldera-forming 2 tephra deposits on the north west caldera wall; e) the tephra and ignimbrite deposits within the caldera-forming 1 sequence of the north west caldera wall; f) the caldera-forming 2 sequences of the north east caldera wall. Photos taken by Louise Goode and Shane Cronin.

3.1.2 Caldera-forming (2) sequence

The Second caldera-forming sequence (known as Caldera-forming 2) begins at the sharp transition above caldera-forming 1 sequence and is dominated by large episodic deposits of lapilli and ash fall units in addition to fine ash pyroclastic density current/surge-style deposits (Fig. 3.2. Col. 1). The lower part of the sequence comprises a 20 to 25 m-thick tephra unit dominated by alternating, weathered, clast-supported bedded lapilli and ash layers. Most of the beds produce normal grading of fine to medium lapilli whereas the ash layers were fine-grained, uniformly graded with thicknesses varying from 2 cm to up to 1 m thick. Intercalated in the bedding was large bombs and obsidian clasts that occurred infrequently throughout the sequence (e.g. T40). Preceding this sequence was a surge-like ash layer that separated the overlying tephra sequence consisting of a 1 to 1.5 m-thick layer of weathered fine ash (Fig. 3.3d). Above this is an ash layer overlain with bedding containing medium to coarse lapilli with interbedded fine ash layering (e.g. T39). The main part of the sequence is dominated by a 20 m-thick sequence of alternating beds of graded medium to coarse lapilli (e.g. T38) and fine ash layers varying from 1 to 50 cm in thickness (Fig. 3.1.3d). Above this lies coarser bedded lapilli and scoria which transitions into a massive scoria unit and interbedded tephra of coarse lapilli (e.g. T35, T36, T37). This sequence is terminated by a 0.5 m-thick fine ash/soil layer comprised of fine ash surge deposits and fine lapilli and a light brown surge coarse ash and soil occurring above this layer (Col. 1).

In the north east caldera wall (Fig. 3.2. Col. 3), the Caldera-forming 2 sequence comprises a 2.5 m thick sequence of bedded, normally graded, coarse lapilli units to fine lapilli and coarse ash units with significant breaks in eruptive phases indicated by large soil units and weathered material. Above the Caldera-forming 2 sequence a there is soil horizon with intercalated charcoal, which transitions into a white, fine ash layer with accretionary lapilli (Fig. 3.1.3f). Above this unit resides bedded lapilli that contains different units of weathered lapilli and interbedded fine ash layer 0.5 m-thick (e.g. T55). The lower segment of this unit consists of medium lapilli unit and the upper segment made up of fine to coarser lapilli unit (e.g. T53, T54). The sequence is overlain by a deposit of fine ash uniformly graded which transitions into the soil horizon and weather ash.

3.1.3 Post Caldera formation sequence

The topmost section in the north west caldera wall is comprised of the post-caldera sequence separated by the before mentioned soil layer. The sequence consists of bedded fine to coarse lapilli with interbedded fine ash layers before terminating into a sequence of fine ash to medium lapilli ash bedding indicative of a surge-style eruption phase (Fig. 3.2. Col. 1). This surge deposit is 1 to 2 m thick and also contains ash deposits with also coarse ash layer interbedded in between the fine to medium ash layers. This ceases with the deposition of tephra bedding that is comprised of fine to coarse lapilli units with interbedded layers of fine to medium ash (e.g. T24, T25). The unit sequence is made up of several different units of tephra indicative of non-sustained eruption phases with tephra units ranging from black scoriaceous lapilli units, fine grey lapilli and interbedded coarse ash (Fig. 3.3c). This is capped with a sequence of pyroclastic surge deposits consisting of fine to medium ash layers and soil horizons formed from the weathering of the different units. Within the sequence some interbedded fine lapilli and coarse lapilli are observed though it is dominated primarily by the fine ash of varying in colouration (due to weathering) and large soil units indicating possible breaks in volcanism. Above this much of the top strata is weathered with the upper most layer capped by top soil (Fig. 3.2. Col. 1).

3.1.4 Outer caldera flank sequence

Around 12 km south west from the TCVC lie deposits of ash and weathered lapilli. Their origin is uncertain but it is likely that the erupted from an outer flank parasitic cone. The outer flank sequence (Fig. 3.2. Col. 2) contains multiple alternating beds of lapilli and ash layers with large soil layers separating units within the sites (Fig. 3.3a). The base of the sequence consists of fine lapilli and scoriaceous material, 0.5 m thick (e.g. T1). Overlain was a thin 1 to 5 cm-thick fine ash layer separating the unit from the bedded tephra of clast supported finer lapilli. This sequence of fine to coarse lapilli with interbedded fine ash layers consisted for 3 m with selected tephra bedding containing normal grading and a range of lapilli sizes (fine to coarse) within a clast supported unit (e.g. T5). The topmost unit of the sequence was dominated by tephra bedded consisting of the to medium to coarse lapilli unit 0.5 m-thick which transitions into weathered soil at the top of the sequence (e.g. T7). Discolouration of the lapilli due to weathering and clays caused yellowing of the ash and lapilli (Fig. 3.3a). The sequence continues transitioning into weathered pyroclastic surge units 2 m-thick comprised of fine to medium ash and fine lapilli with interbedded pumaceious material. This transitions into a soil

and weathered ash horizon. The upper units from the sequence is dominated of weathered coarse scoraceious lapilli, which is overlain by a weathered tephra unit and soil. The sequence is capped by a 30 cm-thick yellow pumice lapilli and black coarse lapilli unit which transitions into weathered tephra and soil.

3.1.5 Intra-caldera (Mt. Batok, Bromo and Sandsea) sequence

Within the caldera resides multiple lava flows and ash deposits that are a product from the several cones that exist inside Tengger. These include active Mount Bromo, Mount Batok, Ajek-Ajek and Jambangan caldera and Semeru (Solikhin et al., 2012). Much of the caldera floor is primarily fall primarily made up of ash and lapilli from more recent volcanic eruptions from the active Mt. Bromo and extinct Mt. Batok (Fig. 3.4a). In areas surrounding cones, lava flows (Fig. 3.4b) exist such as at the base of Mt. Batok (e.g. T49, T50) and the Sandsea floor towards the ancient intra-caldera cones (e.g. T15). Surrounding the northern extent of Bromo massive deposits of tephra (ash and lapilli) exist on the flank extending out from the crater rim (Fig. 3.4c). Activity within the intra-caldera cones only occurs at Bromo infrequently producing degassing events and ash plumes.

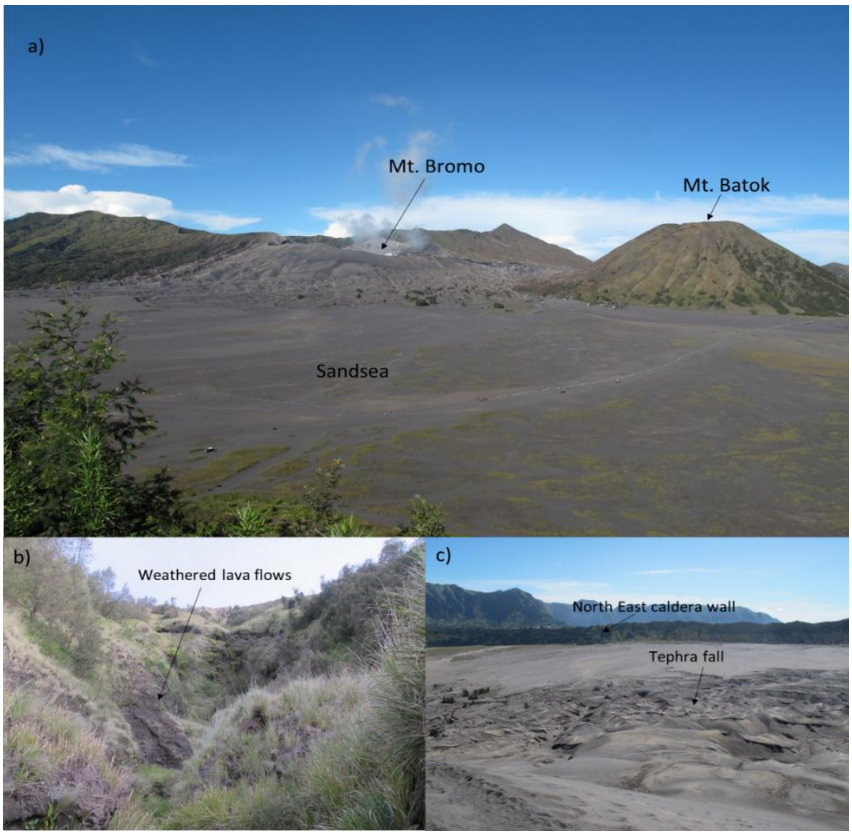

Figure 3.4. Tengger Caldera and its associated intra-caldera, post-caldera volcanic cones: a) Mt. Bromo and Batok with the Sandsea in the foreground. b) Lava flow/s at the base of Mt. Batok. c) Volcanic deposits of ash and lapilli on the flanks of Mt. Bromo with the North East caldera wall in background. Photos taken by Louise Goode and Shane Cronin.

3.2 Petrography and mineralogy

3.2.1 General petrography

The samples from the Tengger-Bromo volcanic complex contains similar mineralogy and petrology between different groups throughout the sequence. Groups were defined by the silica content of the sample and separated into high silica (above 50 wt.%), low silica (below 55 wt.%) groups. The intra-caldera cones Batok and Bromo are grouped separately. Modal compositions of Tengger caldera complex tephra, lava and ignimbrite deposits are shown in Table 3.2 with representative mineral compositions in Table 3.3 to 3.4. Large variation in textures occurring within the lavas at Tengger-Bromo that range from porphyritic textures seen in the lavas from Batok, Sandsea, Bromo and pre caldera sequence lavas to aphyric lapilli of the caldera-forming and post caldera sequences. The majority of the samples contain large phenocrysts of plagioclase, clinopyroxene and orthopyroxene in a groundmass of microlites and glass (lavas) or in glassy matrix (juvenile tephra) (Fig. 3.2.1c and d). The phenocryst abundances range between 20 to 50% with the groundmass constituting 50 to 70% with juvenile lapilli containing more groundmass than the lavas (Table 1). The groundmass of the lavas is comprised of microlites of plagioclase (±oxides) within a fine grained glassy groundmass (Fig. 3.2.1a). Bromo contains larger modal volume of plagioclase (23-36%) with phenocrysts ranging from 1000 to 2500 µm and smaller microcrysts of olivine, clinopyroxene and orthopyroxene in a glassy groundmass (Fig. 3.2.1c). Batok lavas contain phenocrysts of both plagioclase (21-26%; 1000 to 2500 µm in length) and clinopyroxene (11-17%; 500 to 1000 µm in length) in a matrix supported by microlites of olivine, plagioclase, oxide and volcanic glass (46-59%).

Table 3.2: Modal proportions of mineral phases in selected Tengger-Bromo Volcanic Complex rocks.

	Low silica group			Batok		High silica group		Bromo	
	Lava spatter	Lava flow	Lava spatter	Lava	Lava	Lapilli clasts	Lava spatter bomb	Lapilli clast	Lava spatter
Mineral	T44	T48	T63	T49	T50	T24	T47*	T51	T52a
Ol	4	4	2	4	3	4	<1	<1	2
Opx	<1	<1	3	2	3	4	9	7	3
Cpx	4	3	10	17	11	12	17	9	7
Plag	9	18	24	26	21	23	23	23	36
Ox	<1	<1	2	5	4	1	3	3	<1
GM	81	73	59	46	59	56	47	57	51
Amph	-	-	-	-	-	-	<1	-	-

Modal phase volume (%) obtained from 100 to 200 point counts per sample. Ol, olivine; Opx, Orthopyroxene; Cpx, Clinopyroxene; Plag, Plagioclase; Ox, Fe-Ti Oxide; Amph, Amphibole; GM, Groundmass. Groupings based off silica content.

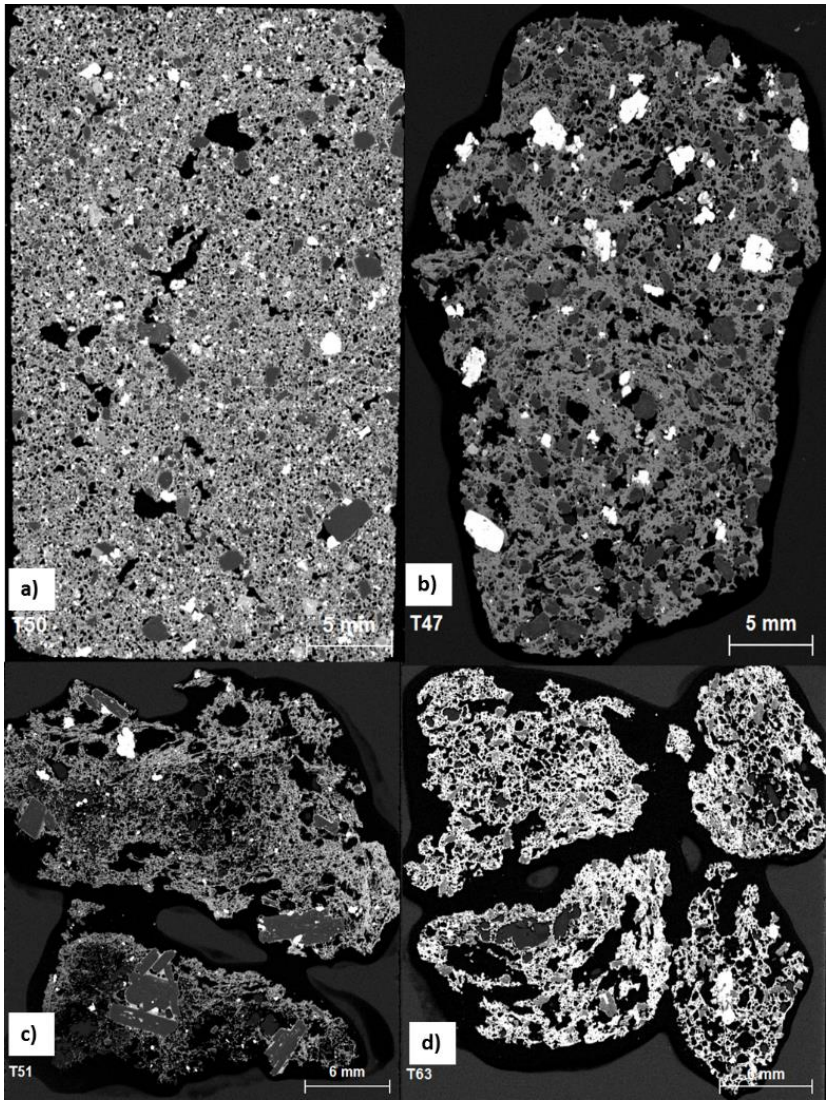

Figure 3.5: Photomicrographs of volcanic deposits of lava, spatter and juvenile lapilli from fall deposits associated with the Bromo and Batok post-caldera volcanic centres and Tengger caldera wall sequences; a) Batok lava (T50); b) NW caldera wall lava spatter bomb (T47); c) Bromo juvenile lapilli (T51) and d) NE caldera wall juvenile lapilli (T63).

3.2.2 Mineral characteristics and compositions

Plagioclase

Plagioclase is the dominant mineral in Tengger-Bromo volcanic complex rocks, occurring as a phenocrysts, microcrysts and microlites. It was found in lapilli and lava, and is generally more weathered (due to the tropical conditions) within the wall lapilli. Within the juvenile lapilli thin sections, the plagioclase is usually the only phenocryst seen usually forming 1000 µm or greater crystals within a glass matrix. Plagioclase within the lavas range from microlites to large phenocrysts (250 µm to 5000 µm in length). The chemical composition of the plagioclase from the caldera wall ranges from An_{62} to An_{95} (Fig. 3.7a). Meanwhile Bromo produces a clear grouping with the core to rims between An_{55} to An_{70} (Fig. 3.7b). The plagioclase in deposits from the caldera-forming and post caldera sequences (high and low silica groups) have a large

variation in the chemical composition with the composition of mid and rims being similar to the range observed in cores, from An_{60} to An_{95} (Fig. 3.6).

Table 3.3: Representative chemical compositions of plagioclase.

Group	Low silica group			Batok		High silica group		Bromo	
Sample	T44	T48	T63	T49	T50	T24	T47	T51	T52a
Grain-position	P3-M	P3-C	P9-R	P2-C	P9-M	P4-M	P3-C	P8-C	P2-C
MgO	0.02	0.03	0.10	0.02	0.02	0.05	0.02	0.08	0.06
Na2O	1.12	1.40	3.67	1.09	1.02	2.75	2.67	4.05	4.30
P2O5	0.22	0.19	0.17	0.22	0.22	0.15	0.19	0.15	0.11
SiO2	44.67	45.90	51.89	45.03	44.66	49.05	48.37	52.51	53.67
Al2O3	33.96	33.38	29.76	34.27	34.46	31.23	31.20	28.94	28.52
Cr2O3	0.01	0.01	0.02	0.00	0.00	0.00	0.00	0.02	-0.02
K2O	0.03	0.03	0.23	0.04	0.03	0.10	0.07	0.57	0.63
TiO2	0.01	0.01	0.04	0.00	0.01	0.02	0.02	0.05	0.03
CaO	18.23	17.46	13.32	17.95	18.48	15.07	15.55	12.17	11.66
NiO	-0.01	0.02	-0.02	-0.02	0.00	0.00	0.00	-0.03	0.02
FeO	0.54	0.71	0.71	0.47	0.48	0.62	0.72	0.62	0.60
Fe2O3	0.60	0.79	0.79	0.52	0.53	0.69	0.80	0.69	0.67
MnO	0.00	0.02	0.01	0.02	0.00	-0.01	-0.01	0.00	0.01
Total	98.80	99.16	99.89	99.08	99.37	99.04	98.79	99.13	99.60
Mg	0.00	0.00	0.01	0.00	0.00	0.00	0.00	0.01	0.00
Na	0.10	0.13	0.32	0.10	0.09	0.25	0.24	0.36	0.38
P	0.01	0.01	0.01	0.01	0.01	0.01	0.01	0.01	0.00
Si	2.09	2.13	2.36	2.10	2.08	2.27	2.25	2.41	2.44
Al	1.87	1.83	1.60	1.88	1.89	1.70	1.71	1.56	1.53
Cr	0.00	0.00	0.00	0.00	0.00	0.00	0.00	0.00	0.00
K	0.00	0.00	0.01	0.00	0.00	0.01	0.00	0.03	0.04
Ti	0.00	0.00	0.00	0.00	0.00	0.00	0.00	0.00	0.00
Ca	0.91	0.87	0.65	0.90	0.92	0.75	0.77	0.60	0.57
Ni	0.00	0.00	0.00	0.00	0.00	0.00	0.00	0.00	0.00
Fe	0.02	0.03	0.03	0.02	0.02	0.02	0.03	0.02	0.02
Mn	0.00	0.00	0.00	0.00	0.00	0.00	0.00	0.00	0.00
Total	5.01	5.00	4.99	5.00	5.01	5.00	5.01	5.00	4.99
An	89.84	87.17	65.83	89.88	90.76	74.73	75.98	60.32	57.75
Ab	9.99	12.65	32.82	9.88	9.06	24.68	23.61	36.32	38.54
Or	0.18	0.18	1.35	0.24	0.18	0.59	0.41	3.36	3.72

Grain: P#, phenocrysts and the number within analysis. Position C, Core; M (Mid-point); R, Rim. An, Anorthite content; Ab, Albite content; Or, Orthoclase content. Structural formula based on 8 oxygens. Representative sample based off median of represented group.

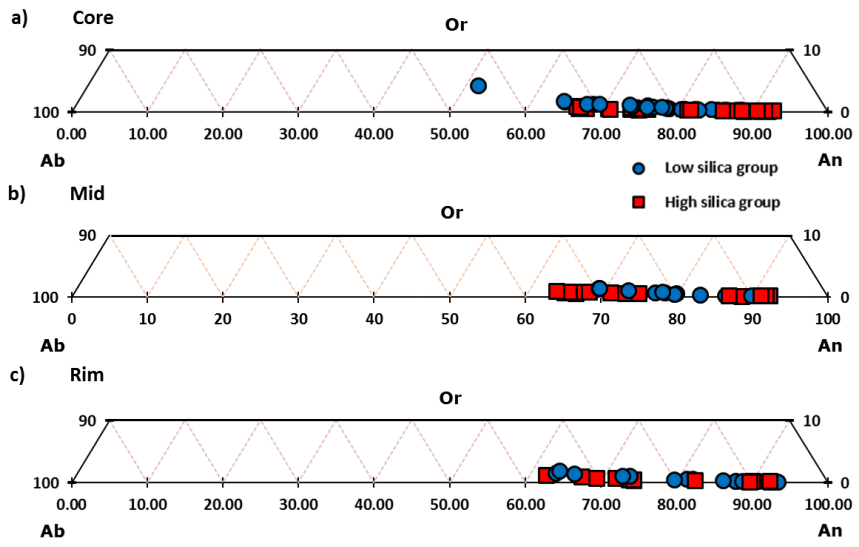

Figure 3.6: Compositional variation in plagioclase phenocrysts within volcanic rocks from the caldera wall/s. a) core position analyses; b) Mid position analyses and c) Rim position analyses. Grouping separated by silica content (High silica, red; Low silica, blue).

Four main types of the plagioclase are observed (Appendix Table A.1). Type 1 consist of plagioclase of no zonation usually greater than 1000 µm in size and tend to have inclusions of melt, titanomagnetite and sometimes olivine. Euhedral to subhedral plagioclase are predominately seen as microlites and microcrysts and rarely as phenocrysts. Type 1 plagioclase is observed usually forming glomerocrysts with clinopyroxene and orthopyroxene.

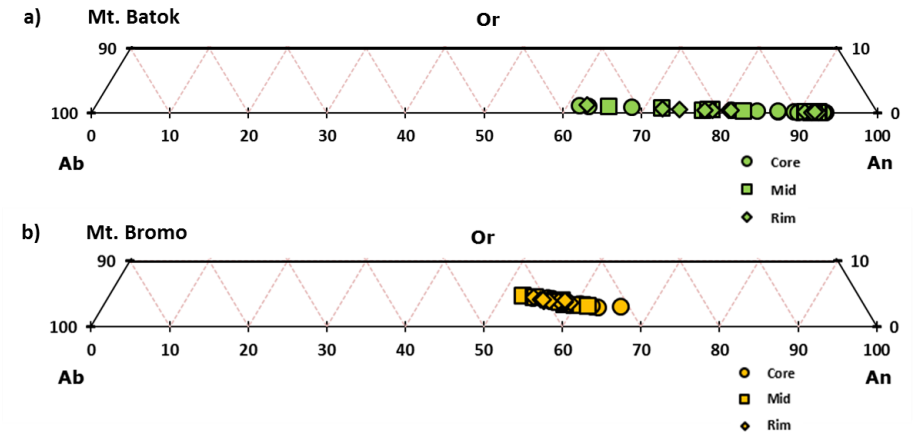

Figure 3.7: Compositional variation in plagioclase phenocrysts in the post-caldera, intra-caldera volcanic rocks: a) Mt Batok and b) Mt. Bromo. Position: Core; circle; Mid, square; Rim, diamond.

Type 2 plagioclase are subhedral with gradual zonation patterns (usually normal zonation decreasing in Ca content from core to rim). This type occurs as single phenocrysts, usually 250 to 4000 µm in length with many of the crystals containing inclusions such as titanomagnetite, melt inclusions, olivine, clinopyroxene and orthopyroxene. Type 2 produces Carlsbad twinning sometimes (T49) in addition to the general lamellar twinning generally associated with plagioclase

Type 3 plagioclase is commonly observed in all rocks showing oscillatory zonation in subhedral crystals. These are either observed within glomerocrysts or as single crystals, 600 µm to 5000 µm in length and containing melt, titanomagnetite, olivine and pyroxene inclusions. Sieved textures cores are present in some crystals.

Type 4 plagioclase is observed within most samples and is defined by reaction rims of lower An# (Fig. 3.6-3.7) producing a well-defined compositional boundary between the core and rim. Common inclusions observed are titanomagnetite and melt. Some of the Type 4 plagioclase show less defined zoning. Lamellar twinning is consistently seen in Type 4 plagioclase with mostly 250 µm to 900 µm subhedral crystals observed.

Clinopyroxene

Augite is the commonly observed clinopyroxene, occurring as phenocrysts, microcrysts and rarely as microlites of euhedral to subhedral grains throughout the caldera complex. The chemistry of augite differs between high and low silica groups and the intra-caldera cones Batok and Bromo. Augite at Batok was higher in magnesium (En ~42-43%) and calcium (Wo ~40-42%) in comparison to Bromo with higher iron content (Fs 21-22%) and lower calcium (Wo 36-37%) (Fig. 3.8). Samples from the caldera wall produced a chemical composition similar to Batok and Bromo (Wo 39-41%; En 40-43%; Fs~16.5-19%) with no variance between the low silica and high silica groupings (Fig. 3.8b and c). Batok showed negative trends associated to increasing iron content compared to calcium whereas Bromo and the caldera wall clustered and produces no clear chemical trends.

Table 3.4: Representative chemical compositions of clinopyroxene.

Group	Low silica group	Batok		Bromo		High silica group	
Sample	T63	T49	T50	T51	T52a	T24	T47
Grain-position	P4-C	P1-C	P2-C	P4-C	P2-C	P5-C	P2-C
MgO	14.59	14.56	15.42	14.18	14.02	15.06	13.90
Na2O	0.29	0.32	0.24	0.25	0.25	0.33	0.35
P2O5	0.20	0.23	0.21	0.20	0.20	0.22	0.16
SiO2	51.20	50.78	51.13	50.95	50.73	50.54	49.59
Al2O3	2.76	2.53	2.40	1.76	1.75	2.66	3.02
Cr2O3	0.02	0.00	0.00	0.01	0.00	0.02	0.00
K2O	0.00	0.00	0.00	0.00	0.00	0.00	0.01
TiO2	0.66	0.64	0.52	0.64	0.56	0.60	0.47
CaO	19.42	19.27	20.62	17.79	18.03	19.28	19.62
NiO	0.00	0.00	0.01	-0.03	-0.01	0.00	0.03
FeO	10.35	10.43	8.74	13.90	13.26	10.42	11.46
Fe2O3	11.50	11.59	9.71	15.45	14.74	11.58	12.74

MnO	0.31	0.38	0.32	0.45	0.43	0.33	0.45
Total	99.79	99.14	99.59	100.10	99.22	99.45	99.06
Mg	0.81	0.82	0.86	0.80	0.80	0.84	0.79
Na	0.02	0.02	0.02	0.02	0.02	0.02	0.03
P	0.01	0.01	0.01	0.01	0.01	0.01	0.01
Si	1.91	1.91	1.91	1.92	1.93	1.90	1.89
Al	0.12	0.11	0.11	0.08	0.08	0.12	0.14
Cr	0.00	0.00	0.00	0.00	0.00	0.00	0.00
K	0.00	0.00	0.00	0.00	0.00	0.00	0.00
Ti	0.02	0.02	0.01	0.02	0.02	0.02	0.01
Ca	0.78	0.78	0.83	0.72	0.73	0.78	0.80
Ni	0.00	0.00	0.00	0.00	0.00	0.00	0.00
Fe	0.32	0.33	0.27	0.44	0.42	0.33	0.36
Mn	0.01	0.01	0.01	0.01	0.01	0.01	0.01
Total	4.01	4.01	4.02	4.02	4.01	4.03	4.04
Wo	40.63	40.42	42.17	36.78	37.65	39.86	40.96
En	42.47	42.50	43.88	40.79	40.74	43.32	40.37
Fs	16.90	17.08	13.95	22.43	21.61	16.82	18.67

Grain: P#, phenocrysts and the number within analysis. Position C, Core; M (Mid-point); R, Rim. Wo, Wollastonite content; En, Enstatite content; Fs, Ferrosilite content. Structural formula based on 6 oxygens. Representative sample based off median of represented group.

Four main types of clinopyroxene phenocryst have been observed with all phenocrysts showing features associated with augite such as single twinning. Additionally the geochemistry shows little chemical variation between crystals within the same locality. Type 1 clinopyroxene contains 250 to 1100 µm with no zonation and inclusions of melt, titanomagnetite and in some cases orthopyroxene where glomerocrysts have formed. Little chemical variation is observed in addition to fracturing usually along cleavage planes. Type 2 crystals are usually 500 µm to 1100 µm in size and are defined by concentric zoning of normal (where the core is Mg rich with Fe rich rims) and reversed zonation. Many exist as single phenocrysts with larger crystals containing inclusions of melt, titanomagnetite and sometimes plagioclase and other pyroxenes. Slight chemical variations are observed within zones and the cores occasionally have sieve textures. The last type (Type 3) has less defined zonation that is commonly observed in small subhedral phenocrysts. Usually weathered and fractured crystals range from 250 µm to 900 µm with inclusions of melt and titanomagnetite observed in larger phenocrysts (T24).

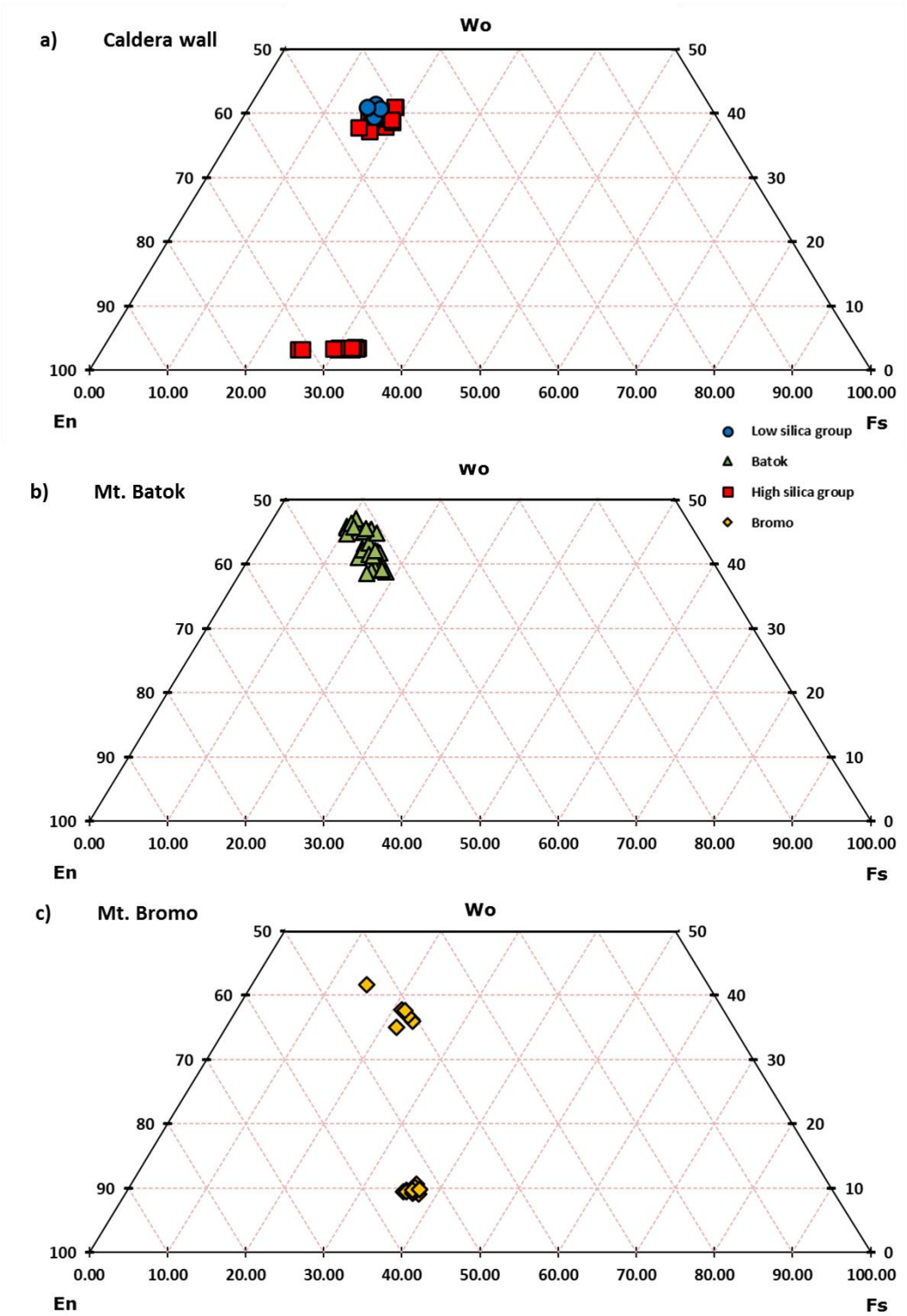

Figure 3.8: Analyses of pyroxene phenocrysts from different localities within the Tengger-Bromo complex; a) Caldera wall; b) Mt Batok and c) Mt. Bromo. Grouping separated by silica content: High silica, red; Low silica, blue; Batok, green; Bromo, gold.

Orthopyroxene and Pigeonite

The Pigeonite and orthopyroxene observed occurs predominately as phenocryst and microcrysts within lavas from Bromo (T51, T52a) and samples from the caldera wall (T47). Between 1 to 4% of orthopyroxene was observed in caldera wall samples. Orthopyroxene in Batok occurring as microcrysts and smaller more weathered phenocrysts with proportions ranging from 4 to 9%. Samples from the Caldera wall (T47) were found to be chemically distinct to orthopyroxene group (En 65.18%; Wo 3.26%; Fs 31.55%) whereas the Bromo contained pigeonite with its higher Ca and Fe content (En~37%; Wo~53%; Fs~37%) (Fig. 3.8c). Small proportions of orthopyroxene was observed in other samples throughout the caldera wall and in Batok samples though occurring as microcrysts and smaller more weathered phenocrysts. Two types of pyroxene (both pigeonite and orthopyroxene) minerals were observed. Type 1 are unzoned and euhedral to subhedral in shape. Most of crystals contained fractures with most having inclusions of melt material or titanomagnetite. Type 2 was different in that a concentric zonation was observed with slight alternating normal (Mg rich core/ Fe rich rim) and reversed zoning. This contains similar textures to the observed Type 1 though this was additionally found to exist in glomerocrysts of plagioclase and clinopyroxene. Overall the Type 2 orthopyroxenes were usually 500 to 1000 µm and Type 1 orthopyroxene was more commonly 250 to 2500 µm.

Table 3.5: Representative chemical compositions of orthopyroxene and pigeonite.

Group	High silica group	Bromo	
Sample	T47	T51	T52a
Grain-position	P3-C	P1-C	P1-M
MgO	23.70	18.73	18.24
Na2O	0.03	0.11	0.10
P2O5	0.01	0.04	0.07
SiO2	52.43	51.69	51.32
Al2O3	0.94	0.99	1.07
Cr2O3	0.00	-0.01	0.01
K2O	0.00	0.00	0.00
TiO2	0.16	0.32	0.34
CaO	1.65	4.48	4.72
NiO	-0.04	0.02	0.02
FeO	20.45	22.77	22.98
Fe2O3	22.73	25.31	25.54
MnO	0.75	0.74	0.69
Total	100.09	99.87	99.56
Mg	1.31	1.06	1.04
Na	0.00	0.01	0.01

P	0.00	0.00	0.00
Si	1.95	1.96	1.96
Al	0.04	0.04	0.05
Cr	0.00	0.00	0.00
K	0.00	0.00	0.00
Ti	0.00	0.01	0.01
Ca	0.07	0.18	0.19
Ni	0.00	0.00	0.00
Fe	0.63	0.72	0.73
Mn	0.02	0.02	0.02
Total	4.03	4.01	4.01
Wo	3.26	9.27	9.83
En	65.18	53.94	52.83
Fs	31.55	36.79	37.34

Grain: P#, phenocrysts and the number within analysis. Position C, Core; M (Mid-point); R, Rim. Wo, Wollastonite content; En, Enstatite content; Fs, Ferrosilite content. Structural formula based on 6 oxygens. Representative sample based off median of represented group.

Olivine

Small amounts of olivine have been observed in the intra-caldera cones and in the caldera wall samples with modal proportions varying 1% to 4% within sampled lavas. Primarily occurring as a minor mineral or inclusion within most samples with generally occurs as subhedral to anhedral crystals (<100 µm). Larger grains of euhedral (500 - 1000 µm) are seen in samples of lava from Batok (T50) and the lavas from the North western (T48) caldera walls. Sometimes skeletal texture olivine is observed with the crystals lack inclusions or chemical variations. Weathering and alteration to iddingsite is sometimes seen on crystal edges especially in the weathered lava at the base of the caldera wall (T49).

Table 3.6: Representative chemical compositions of olivine.

Group	Low silica group			Batok	High silica group	Bromo
Sample	T44	T48	T63	T50	T24	T52a
Grain-position	P1-C	P2-C	P1-C	P4-C	P2-C	P1-C
MgO	35.71	34.77	32.94	35.84	34.25	26.03
Na_2O	0.00	0.00	0.01	0.01	0.02	0.01
P_2O_5	0.01	0.01	0.02	0.01	0.01	0.07
SiO_2	37.30	37.40	37.35	37.54	36.92	35.02
Al_2O_3	0.03	0.03	0.01	0.00	0.02	0.04
Cr_2O_3	0.00	0.00	0.00	0.00	0.00	0.00
K_2O	0.00	0.00	0.00	0.01	0.00	0.00
TiO_2	0.01	0.01	0.01	0.01	0.00	0.03
CaO	0.20	0.19	0.21	0.15	0.13	0.27
NiO	0.05	0.05	0.04	0.00	0.03	0.01
FeO	27.05	27.08	29.31	26.54	28.83	37.60
Fe_2O_3	30.06	30.10	32.57	29.50	32.04	41.79
MnO	0.48	0.47	0.53	0.46	0.53	0.74

Total	100.84	99.98	100.44	100.51	100.74	99.82
Mg	1.41	1.38	1.32	1.41	1.36	1.10
Na	0.00	0.00	0.00	0.00	0.00	0.00
P	0.00	0.00	0.00	0.00	0.00	0.00
Si	0.99	1.00	1.00	0.99	0.99	0.99
Al	0.00	0.00	0.00	0.00	0.00	0.00
Cr	0.00	0.00	0.00	0.00	0.00	0.00
K	0.00	0.00	0.00	0.00	0.00	0.00
Ti	0.00	0.00	0.00	0.00	0.00	0.00
Ca	0.01	0.01	0.01	0.00	0.00	0.01
Ni	0.00	0.00	0.00	0.00	0.00	0.00
Fe	0.60	0.60	0.66	0.59	0.64	0.89
Mn	0.01	0.01	0.01	0.01	0.01	0.02
Total	3.01	3.00	3.00	3.01	3.01	3.01
Fo	70.18	69.59	66.70	70.65	67.92	55.24
Fa	29.82	30.41	33.30	29.35	32.08	44.76

Grain: P#, phenocrysts and the number within analysis. Position C, Core; M (Mid-point); R, Rim. Fo, Forsterite content; Fa, Fayalite content. Structural formula based on 4 oxygens. Representative sample based off median of represented group.

The olivine phenocrysts contain varied Mg# values (55 to 80) with the caldera wall ranges from 60 to 70 (T24 ~68; T44 ~70; T48 ~70; T63 ~67) (Fig. 3.9). Mount Batok fairly high Mg content up to Fo_{70} while Bromo has a Mg# of 55 (Table 3.4).

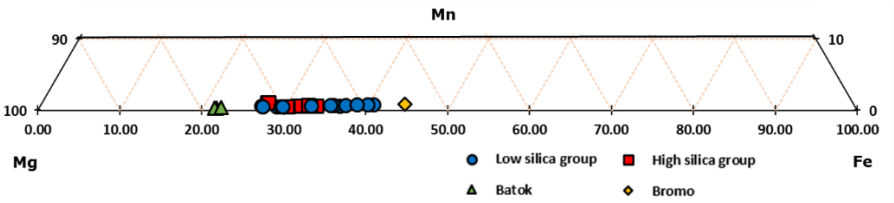

Figure 3.9: Mg-Mn-Fe olivine diagram. Grouping separated by silica content: High silica, red; Low silica, blue; Batok, green; Bromo, gold.

Amphibole and oxides

A single, subhedral amphibole, 900 µm in length, with inclusions of titanomagnetite and melt was observed in sample T47 from the high silica group existing with the caldera-forming sequence. Oxides such as titanomagnetite (1-4 vol. %) are predominantly observed individually in lavas found within the inter-caldera cones and the caldera-forming events. The oxides also can occur as microcrysts and microlites (200 µm to <100 µm in length) within the groundmass or as inclusions within plagioclase, clinopyroxene, pigeonite orthopyroxene.

3.3 Geochemistry

3.3.1 Major element variations

Major and trace element data are reported in Table 3.5 with their respective rock type and locality. Samples with LOI values higher than 2 wt% and those that produced abnormally high chemical weathering and alteration index values (greater than 65%) were removed from the dataset as these were considered too weathered (see Appendix). Two different SiO2 groups can be differentiated from the samples analysed: less than 54% and greater than 56 wt% SiO_2. The intra-caldera cones, Batok and Bromo lie within the low SiO_2 and high SiO_2 groups, respectively. On the diagrams presented in this thesis, Batok, Bromo and Sandsea volcanic rocks are further identified from the low and high silica groups to investigate spatial variations in geochemistry within the complex. In a total alkali versus silica diagram (Fig.3.10a), the volcanic rocks in the low silica group lie in the basalt to basaltic andesite fields and the high silica group rocks lie in the basaltic trachy-andesite to trachy-andesite fields. The rocks from Batok are basaltic andesites and rocks from Bromo and the Sandsea lavas lie in the trachy-andesite. T47 sits as an outlier, but was plotted due to its importance within the stratigraphy (a lower unit of the caldera-forming sequence). The TCVC volcanic rocks are medium-K (low silica group including Batok) and high-K (high silica group including Bromo and the Sandsea) (Fig. 3.10b) with most rocks lying in the tholeiitic fields in Figs.3.10c and d. The TCVC volcanic rocks are medium-K (low silica group including Batok) and high-K (high silica group including Bromo and the Sandsea) (Fig. 3.10b) with most rocks lying in the tholeiitic fields in Figs.3.10c and d.

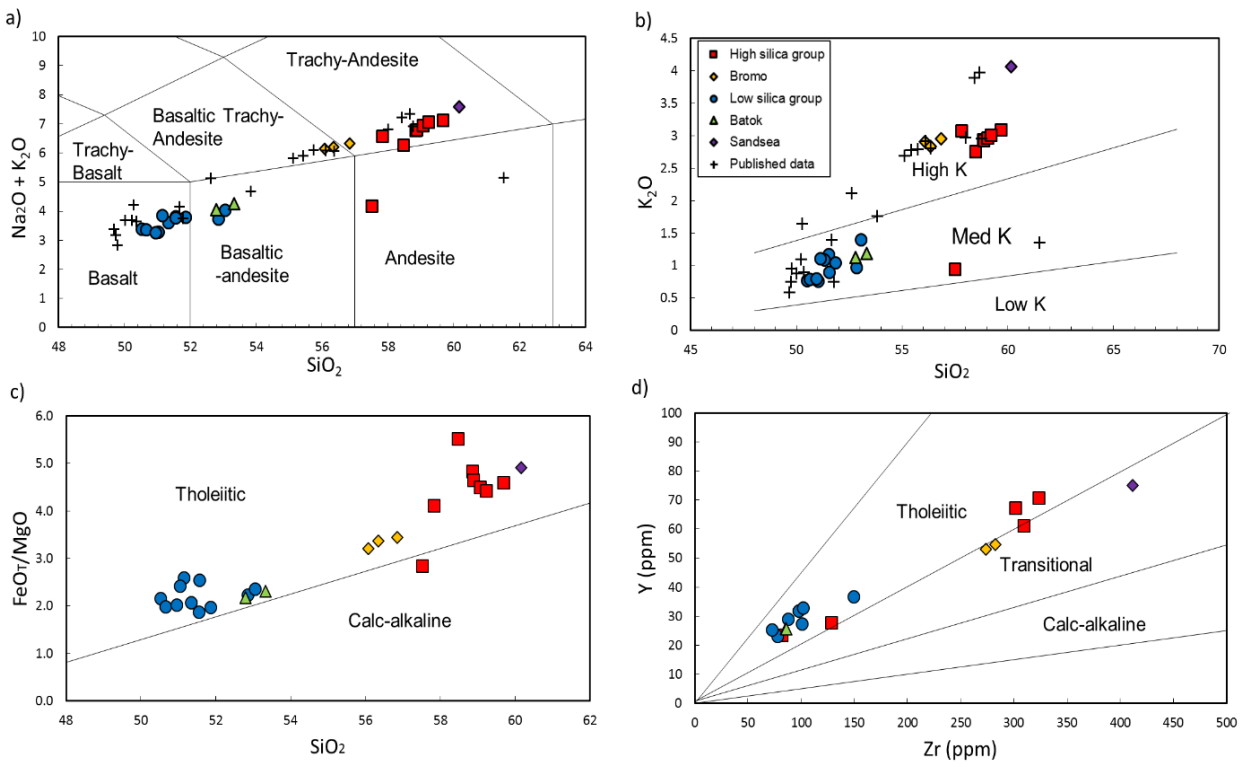

Figure 3.10: Diagrams indicating rock type and other discriminating factors for samples: a) TAS diagram showing analyses of Tengger Caldera volcanic rocks by Van Gerven and Pichler (1995); b) K_2O versus SiO_2 discrimination for low, medium and high K sub-alkaline rocks series by Maitre et. al. (1989); c) subdivision of tholeiitic and calc-alkaline series after Miyashiro (1974) (FeOt = 0.9 x Fe_2O_3 + FeO); d) Zr versus Y plot characterising their tholeiitic, transitional and calc-alkaline nature after Maclean and Barrett (1993).

Table 3.7: Whole rock major element and trace element concentrations of Tengger Caldera Volcanic Complex.

Locality	High silica Group												Low silica group														Mt. Batok		Mt. Bromo			Sandsea
Sample no.	T1	T5	T6	T12	T24	T36	T37	T38	T39	T40	T47	T55	T4	T14	T25	T31	T32	T35	T42	T43	T44	T45	T46	T48	T59	T63	T49	T50	T51	T52a	T52b	T15
SiO_2	59.12	57.41	57.32	59.68	58.47	58.85	58.89	59.07	57.97	59.23	57.52	57.83	52.84	52.85	52.86	51.55	51.34	51.86	49.34	51.15	50.52	51.04	50.65	51.56	50.96	53.05	53.34	52.79	56.08	56.35	56.85	60.17
Al_2O_3	15.59	16.61	16.52	16.25	16.29	16.47	16.36	16.35	16.83	16.41	19.54	16.74	19.17	18.15	19.32	19.63	18.94	19.05	19.50	17.92	18.97	18.83	18.55	19.18	19.34	18.31	19.20	19.22	17.53	18.14	18.01	15.92
Na_2O	3.54	3.07	2.93	4.03	3.52	3.84	3.87	3.97	3.63	4.06	3.23	3.50	2.80	2.59	2.75	2.63	2.51	2.73	2.39	2.74	2.62	2.52	2.57	2.87	2.45	2.63	3.06	2.94	3.23	3.38	3.37	3.53
MgO	1.46	1.47	1.37	1.93	1.61	1.85	1.94	2.00	1.86	2.03	2.66	2.30	3.91	4.17	4.26	5.13	4.97	4.96	3.20	4.49	5.30	4.51	5.43	4.38	4.85	4.25	4.23	4.43	2.91	2.67	2.67	1.82
P_2O_5	0.47	0.44	0.43	0.61	0.50	0.60	0.59	0.62	0.57	0.63	0.32	0.53	0.19	0.24	0.18	0.15	0.14	0.15	0.24	0.38	0.27	0.28	0.28	0.29	0.15	0.24	0.20	0.19	0.47	0.44	0.46	0.60
TiO_2	1.08	1.17	1.17	1.14	1.16	1.15	1.14	1.17	1.17	1.17	0.58	1.09	0.92	0.92	0.83	0.75	0.80	0.76	1.34	1.35	1.06	1.03	1.02	1.13	0.86	0.98	0.91	0.88	1.02	0.98	1.02	1.05
CaO	4.09	3.87	3.77	4.88	4.23	4.71	4.83	4.95	4.68	5.03	7.93	5.79	8.51	7.96	8.55	9.42	8.49	8.89	8.39	9.33	9.97	9.71	9.77	9.56	9.30	8.03	8.98	9.21	7.07	7.26	7.02	5.03
K_2O	3.06	2.49	2.52	3.09	2.75	2.93	2.93	2.97	2.79	3.01	0.94	3.07	1.03	1.25	0.97	1.17	1.08	1.05	0.70	1.10	0.77	0.76	0.79	0.89	0.80	1.40	1.19	1.12	2.91	2.83	2.95	4.06
Fe_2O_3	8.33	9.10	9.02	8.90	8.91	8.96	9.01	8.99	9.25	8.99	7.57	9.46	9.76	10.01	9.51	9.61	10.29	9.82	11.36	11.67	11.42	10.90	10.79	11.15	9.83	10.03	9.76	9.64	9.32	9.00	9.18	8.92
MnO	0.18	0.19	0.19	0.19	0.20	0.19	0.19	0.19	0.20	0.19	0.18	0.18	0.18	0.18	0.18	0.16	0.18	0.18	0.20	0.21	0.20	0.20	0.20	0.20	0.19	0.18	0.19	0.18	0.17	0.16	0.16	0.17
LOI	3.28	5.05	5.71	0.09	1.55	1.17	0.91	0.53	1.98	-0.21	0.13	0.38	3.22	2.23	1.20	0.17	1.68	1.20	3.93	0.52	-0.19	0.63	0.43	-0.12	1.86	1.61	-0.21	0.07	-0.31	-0.31	-0.51	-0.40
Total	100.21	100.88	100.95	100.79	99.20	100.73	100.67	100.81	100.92	100.54	100.59	100.86	102.52	100.53	100.61	100.37	100.42	100.64	100.61	100.86	100.92	100.42	100.49	101.09	100.59	100.72	100.83	100.68	100.40	100.91	101.18	100.88
CIW	59.3	63.7	64.2	57.5	60.8	58.9	58.5	57.9	60.2	57.6	61.8	57.5	60.8	60.6	61.2	59.8	61.0	60.0	62.9	57.6	58.7	59.2	58.6	59.0	60.6	60.3	59.2	59.1	57.0	57.4	57.4	55.8
CIA	67.1	70.5	71.1	64.6	67.8	65.8	65.3	64.7	66.9	64.4	63.7	64.3	62.9	63.2	63.1	62.0	63.2	62.1	64.4	59.8	60.1	60.6	60.0	60.7	62.2	63.2	61.5	61.3	63.0	63.0	63.4	65.0
Li				22	10					21	11.9	19.3	21				9.3	8.5	11		8.2	9.3		9.2	9.1	11.7	9.8	9.4	16.8	17.7		23
Be				2.7	1.0					2.6	1.3	2.5	2.7				1.0	0.9	1.2		1.0	1.1		1.2	1.0	1.3	1.1	1.1	2.1	2.2		3.1
Sc				26	31					26	15	26	26				35	31	35		34	38		38	37	33	33	34	25	25		23
Ti				8022	6236					7996	4225	7745	7895				5729	5060	9462		7267	7529		8124	6315	6711	6655	6595	6998	6935		7291
V				60	262					68	113	122	42				242	235	222		297	311		327	251	238	293	301	148	139		79
Cr				7.0	19.6					8	11	8	6.3				34	27	18		27	34		25	55	27	20	23	17	15		6.5
Mn				1612	1473					1625	1581	1591	1673				1602	1454	1680		1658	1781		1770	1661	1573	1603	1636	1408	1384		1465
Co				16	24					17	18	19	15				37	33	33		35	36		35	33	33	28	31	22	22		16
Ni				2	8					3	8	5	1				33	27	19		29	25		22	23	26	10	13	11	11		4
Cu				64	41					70	55	162	70				124	96	187		161	190		161	73	128	43	57	166	175		165
Zn				117	81					116	96	100	116				86	74	103		90	99		108	84	90	87	89	89	89		104
Ga				22	20					22	23	21	22				20	19	22		20	21		23	21	20	21	22	20	22		21
Rb				112	27					108	27	128	101				42	30	23		19	20		24	26	51	32	31	115	120		174
Sr				375	514					371	532	418	332				487	475	470		551	546		545	569	468	563	571	404	457		329
Y				71	24					67	28	61	69				27	23	42		29	32		33	25	37	26	26	53	55		75
Zr				323	82					302	128	309	334				101	78	129		88	98		102	73	149	85	86	274	283		411
Nb				13	3					12	6	12	13				3	3	6		4	4		5	3	5	4	4	11	11		16
Mo				3.6	0.8					3	1	4	3.1				1	1	1		1	1		1	1	2	1	1	3	3		4.9
Cd				0.1	0.1					0.1	0.1	0.1	0.1				0.1	0.1	0.2		0.1	0.2		0.1	0.1	0.1	0.1	0.1	0.1	0.1		0.1
Cs				8.7	1.7					8.2	1.9	11.1	9.1				3.4	2.6	1.9		1.5	1.7		1.2	1.5	4.0	1.8	1.8	9.7	9.9		14.7
Ba				1441	421					1299	707	1205	1435				613	530	698		585	629		681	440	771	497	486	1024	1050		1365
La				38	12					35	17	35	37				11	10	15		11	13		15	11	18	13	13	30	31		43
Ce				83	24					77	36	76	86				23	20	36		26	29		31	23	38	28	27	66	67		93
Pr				11	3					10	5	10	11				3	3	5		4	4		5	3	5	4	4	9	9		12
Nd				46	14					44	19	42	45				14	12	22		16	18		20	14	22	15	15	36	37		51
Sm				11.4	3.5					10.9	4.4	10.5	11.1				3.7	3.1	5.8		4.3	4.7		5.2	3.6	5.5	3.9	3.9	9.0	9.1		12.4
Eu				2.8	1.2					2.7	1.5	2.4	2.7				1.2	1.2	1.9		1.5	1.6		1.7	1.3	1.6	1.4	1.4	2.0	2.1		2.4
Tb				1.9	0.6					1.9	0.7	1.8	1.9				0.7	0.6	1.1		0.8	0.8		0.9	0.7	1.0	0.7	0.7	1.5	1.5		2.1
Gd				12.0	3.8					11.7	4.6	11.3	11.8				4.2	3.5	6.8		4.8	5.2		5.8	4.1	6.0	4.3	4.2	9.5	9.6		13.0
Dy				11.4	3.7					11.1	4.3	10.7	11.3				4.2	3.5	6.6		4.7	5.1		5.6	4.0	5.8	4.1	4.1	9.0	9.1		12.3
Ho				2.5	0.8					2.4	0.9	2.3	2.4				0.9	0.8	1.4		1.0	1.1		1.2	0.9	1.2	0.9	0.9	1.9	1.9		2.6
Er				7.0	2.3					6.7	2.7	6.4	6.9				2.6	2.2	4.0		2.9	3.1		3.4	2.5	3.6	2.5	2.5	5.3	5.4		7.4
Yb				6.4	2.1					6.3	2.7	6.0	6.3				2.5	2.0	3.7		2.7	2.9		3.1	2.3	3.3	2.4	2.3	4.9	5.0		6.9
Lu				1.0	0.3					0.9	0.4	0.9	0.9				0.4	0.3	0.6		0.4	0.4		0.5	0.3	0.5	0.4	0.4	0.7	0.7		1.0
Hf				8.2	2.0					8.0	3.1	8.8	8.6				2.6	2.0	3.4		2.3	2.5		2.8	1.9	3.9	2.2	2.2	7.4	7.6		10.8
Ta				0.8	0.2					0.8	0.4	0.9	0.8				0.2	0.2	0.4		0.2	0.3		0.3	0.2	0.4	0.2	0.2	0.7	0.7		1.0
Th				15.5	3.1					15.3	3.2	21.3	16.7				4.6	3.7	3.2		2.0	2.1		2.6	2.7	6.8	3.4	3.4	17.1	17.3		26.0
U				3.7	0.8					3.7	0.8	5.2	3.6				1.1	0.9	0.7		0.5	0.6		0.7	0.7	1.6	0.9	0.9	4.2	4.2		6.3

Major element concentrations in wt.%; trace element concentrations in ppm. Abbreviations: LOI, Loss On Ignition; CIW, Chemical index of weathering; CIA, Chemical index of alteration. The equations for calculating CIW and CIA have been added to the appendix.

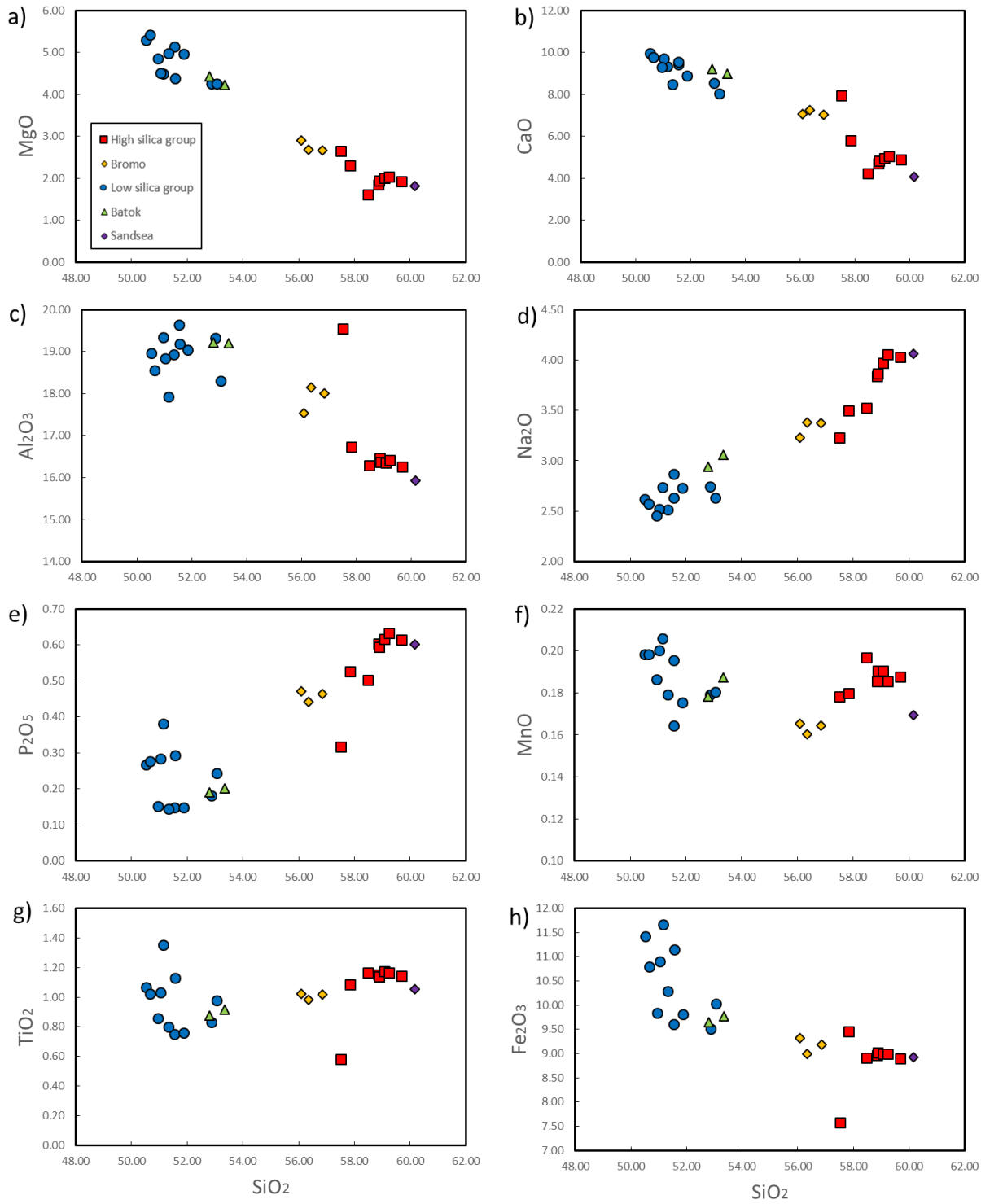

Figure 3.11: Major element variation diagrams for samples obtained from Tengger Caldera.

When plotted against silica content, major elements produce pronounced correlations and trends within the groups. Negative correlations are seen in Al_2O_3, MgO, CaO against SiO_2 (Fig. 3.3.2a-c) with low silica groups producing high concentrations of these elements compared to

the high silica group and Bromo. Fe_2O_3 produces less prominent negative correlation (Fig. 3.11h). Na_2O and K_2O show positive correlation when comparing all samples from Tengger with positive trends between the low silica and high silica groups (Fig. 3.11d). A similar relationship seen in the intracaldera cones with Batok having low concentrations of Na_2O and K_2O compared to Bromo (Fig. 3.11d) and (Fig. 3.10a). Positive correlations are seen in P_2O_5 (Fig. 3.11e). A negative correlation can be seen when TiO_2 is plotted against SiO_2 in the low silica group and Batok group, whereas Bromo and the High silica group produced a positive correlation (Fig. 3.11g). MnO shows a poor correlation with SiO_2 (Fig. 3.11f) with a scattered flat trend observed from the different groups. Bromo (high SiO_2) and Batok (low SiO_2) deviate little from the trends observed over the entire caldera system forming to distinct groups.

3.3.2 Trace element variations

Trace elements established in Fig. 3.12 pertain close relationships to the silica content with positive linear trends observed when comparing to most rare earth elements (REE). This trend is particular evident in light REE and HREE where positive trends are observed with high concentrations observed in the lavas and tephra at Tengger with the Sandsea lava (SiO_2 = 60.17 wt%) producing the usually highest concentrations within the entire system (La=10-40ppm; Ce = 20-90 ppm). This trend continues for heavy REE (Fig. 3.12a-b) with high concentrations occurring with more evolved samples (high silica group and Bromo) (Y = 25-75 ppm; Yb = 2-7 ppm) The general trend is similarly seen in high field strength elements (HFSE) with more evolved material contain high concentrations of HFSE (Fig. 3.12d) though producing a more scattered less prominent positive trend (Hf = ~2-10 ppm). The large ion lithophile elements (LILE) also produces high concentrations however contains well defined trends of mixed positive and negative correlations as observed in Ba (Ba = 400-1400 ppm) and Sr (Sr = 300-550) respectively (Fig. 3.12f-g).

N-MORB normalised multi-element spidergrams (Fig. 3.13) of the Tengger samples show variations in signatures between the compositional groups. General trends show enrichment in LREE (La, Ce, Pr and Nd) when compared to N-MORB. In addition to enrichment of HFSE (Th, U, Nb and Ta) and LILE (Rb and Ba) confirming what is seen in Fig. 3.12. Meanwhile most samples show distinct depletion in Ti and HREE producing relatively standard flat profiles but generally more enriched compared to N-MORB concentrations.

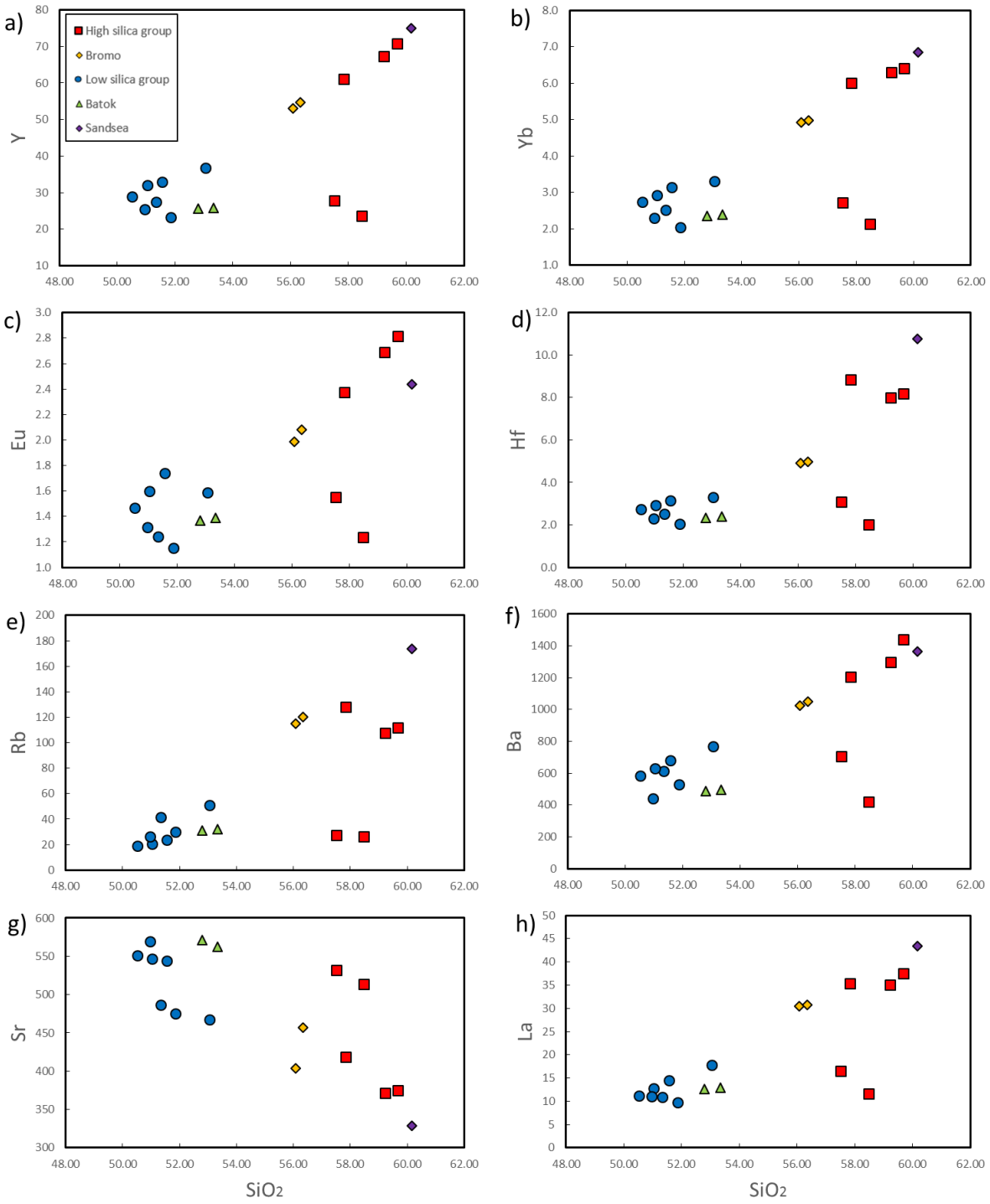

Figure 3.12: Selected trace element variations with SiO_2 for samples from Tengger caldera volcanic rocks.

The high silica group generally contain higher concentrations of trace elements (excluding Sr) compared to samples from the lower silica group. Each group produces their own unique variations in trace elements as seen in Sr, Ba, Ti, Eu, Hf and Tb. The lower silica group produces sharp enrichment patterns in Sr, Ba and Eu. Batok samples and with T24 and T47 from the high silica group producing the same trends (Fig. 3.13a). The High silica group (Fig.

3.13b) shows relatively depleted Sr, while Bromo and Sandsea lavas are relatively depleted in Sr, Hf and other HFSE (Fig. 3.13a). Batok is shown to be enriched additionally by Eu and Ba. Overall each silica group and their associated intracaldera cone follow similar patterns in concentrations relative to N-MORB with predominant fluctuations occurring in Eu, Sr and Ti occurring with only two samples, T24 and T47, do not conform to this relationship. This trend is also observed when comparing the multi-element diagrams to chondrite normalised REE spidergrams (Fig. 3.13c-d); the higher silica samples are generally more enriched and show Eu depletion (Fig. 3.13a). Whereas lower silica samples are less enriched in REE.

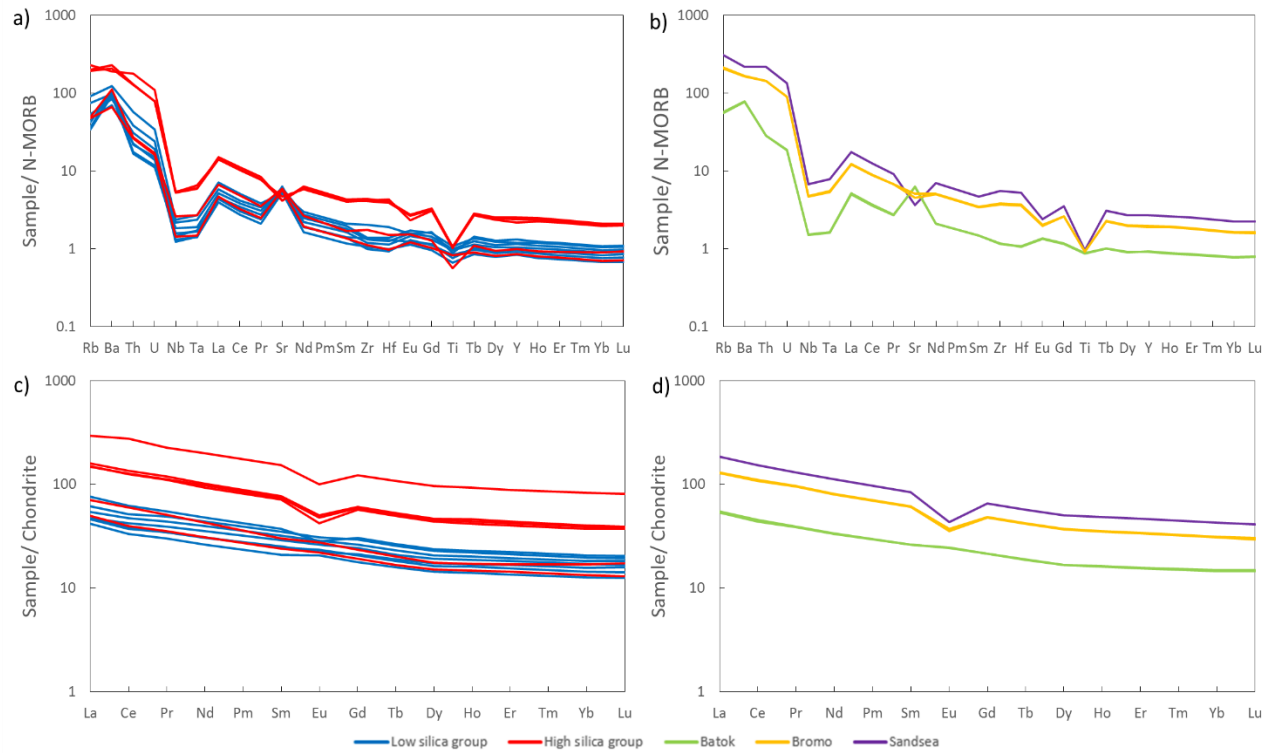

Figure 3.13: (a-b) N-MORB-normalised multi-element diagrams of a) the low and high silica groups; b) the intracaldera cones Batok, Bromo and the Sandsea lava. (c-d) Chondrite (C1) normalised Rare earth element diagrams of c) the low and high silica groups; d) the intracaldera cones Batok, Bromo and the Sandsea lava. Grouping separated by silica content: High silica, red; Low silica, blue; Batok, green; Bromo, gold. Chrondrite and N-MORB values from McDonough, W., and Sun, S. (1995).

Chapter 4: Discussion

4.1 Determination of pre-eruptive magma storage conditions

4.1.1 Pyroxene pre-eruptive pressure and temperature estimates

Two pyroxene thermobarometry

The compositions of touching and non-touching clinopyroxene and orthopyroxene minerals were used to estimate pressure and temperature the two pyroxene thermobarometer developed by Putirka (2008). Only the touching (and non-touching) pyroxene pairs from T47 (caldera forming sequence/high SiO_2) satisfied the test for equilibrium K_D (Fe-Mg) yield K_D values from 0.952 to 1.221, (n = 56) (Fig. 4.1a); The intracaldera cone Bromo samples (T51, T52a) did not satisfy the K_D (Fe-Mg) equilibrium tests indicating that the crystals are not equilibrium (K_D (Fe-Mg) =1.09±0.14) (Fig. 4.1a). Using thermometers (Equation 36 standard deviation (σ) = ±66.5) and barometers (Eq. 39, σ = ±3.2 kbar) the two pyroxene assemblages record a range from 991.4°C to 1151.8°C (average = 1060.6°C, n = 56, σ = ±66.5°C) with the pressure ranging from 4.3 kbar to 13.2 kbar (average = 8.3 kbar, n = 56, σ = ±2.8 kbar) (Fig. 4.1b). It is evident that there are two groupings; one at lower pressure (P) and temperature (T), and another at higher P and T.

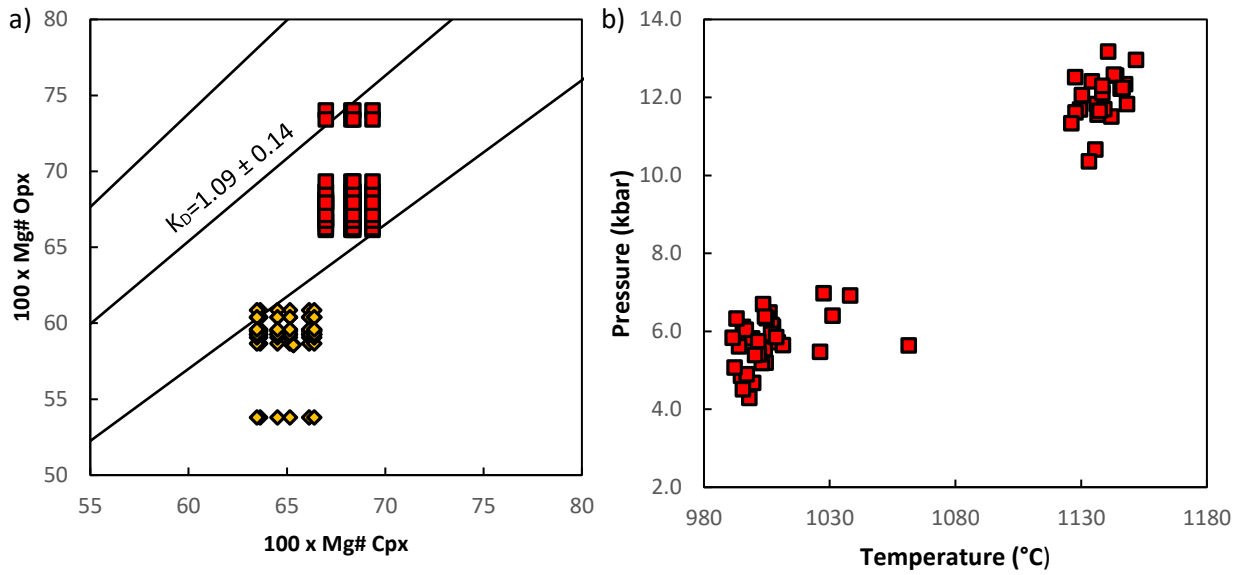

Figure 4.1: a) Test for equilibrium using K_D (Fe-Mg) satisfying 1.09±0.14 between the clinopyroxene and glass groundmass of the respective sample from Putirka (2008) thermobarometry. b) Pressure versus temperature estimation for the pyroxene pairs from high silica group (T47).

Clinopyroxene-melt thermobarometry estimates

Clinopyroxene melt thermobarometry developed by Putirka (2008) (Eq.32 c and d) was used to ascertain the pressure (σ = ±1.4kbar) and temperature (σ = ±45°C) due to the improved accuracy over previous iterations (from Putirka 2003). A water content of 4 wt.%. was assumed for the melt phase for arc magmas as inferred by Plank et al., (2013). The compositions of clinopyroxene and the respective glass groundmass for each sample was used within the high silica (T24, T47, T51, T52a) and low silica (T44, T48, T49, T50, T63) content groups. A test for equilibrium between the clinopyroxene and glass was conducted to establish which phases are in equilibrium with the groundmass composition. Composition combinations with K_D (Fe-Mg) of 0.28±0.08 were assumed to best represent equilibrium with the melt.

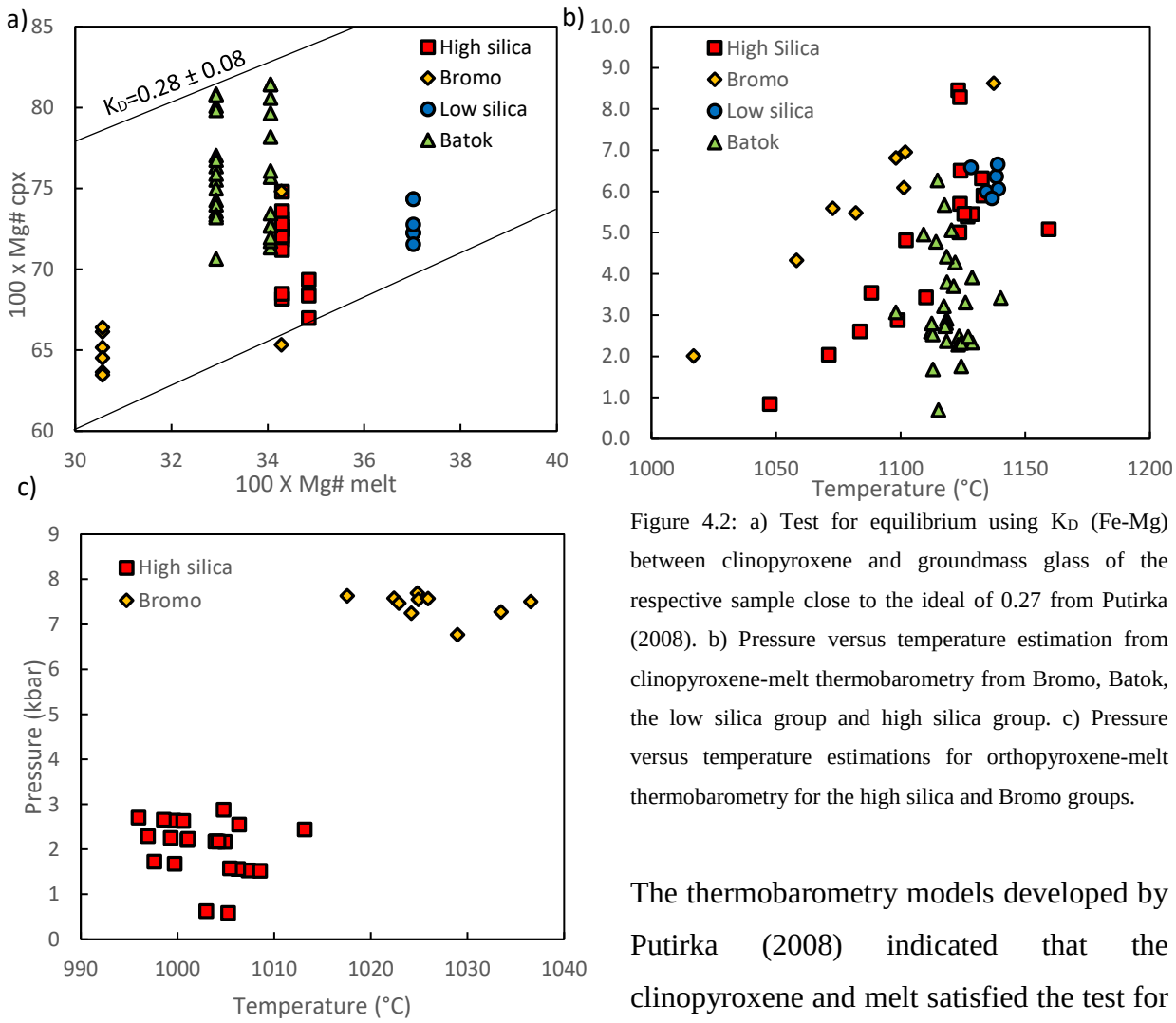

Figure 4.2: a) Test for equilibrium using K_D (Fe-Mg) between clinopyroxene and groundmass glass of the respective sample close to the ideal of 0.27 from Putirka (2008). b) Pressure versus temperature estimation from clinopyroxene-melt thermobarometry from Bromo, Batok, the low silica group and high silica group. c) Pressure versus temperature estimations for orthopyroxene-melt thermobarometry for the high silica and Bromo groups.

The thermobarometry models developed by Putirka (2008) indicated that the clinopyroxene and melt satisfied the test for equilibrium producing K_D (Fe-Mg) ranging from 0.23 to 0.26 (n = 61) (Fig. 4.2a). This indicated that melt compositions with Mg# between 30 and 37 were in equilibrium with clinopyroxene.

The Putirka (2008) models yield temperature estimates for the clinopyroxenes from Batok of 1098-1140°C (average = 1119°C, n = 29, σ = ±7.6°C). The pressure estimates from the barometry modelling for Batok range 0.7 to 6.3 kbar (average = 3.3 kbar, n = 29, σ = ±1.6 kbar). Batok produced wide range of pressure over relatively restricted range in temperature (Fig.4.2b). When looking at the low silica group (T63), which Batok is a part of, the temperature and pressure estimations trend to be higher with the temperature estimates ranging 1128-1136°C (average = 1136°C, n = 6, σ = ±4.2°C) while the pressure estimates are 5.8-6.7kbar (average =6.3 kbar, n = 6, σ = ±0.3 kbar). The estimates for Batok and the low silica group associated groups indicate similar crystallisation temperatures however the low silica group show less variation in pressure than those observed at Batok (Fig. 4.2b).

The clinopyroxenes from Bromo and the high silica group produce temperature estimates of 1017-1137°C (average = 1083.52°C, n = 8 , σ = ±35.8°C). The pressure estimates for Bromo were evenly distributed with pressures ranging from 5.8 to 8.6 kbar (average = 6.61 kbar, n = 8, σ = ±0.9 kbar). The high silica group yielded similar temperature estimates with a range of 1047-1159°C (average = 1112°C, n = 18, σ = ±26.5°C) and pressure estimates ranging from 0.8-8.5 kbar (average = 4.9 kbar, n = 18, σ = ±2.0 kbar). The pressure estimates between Bromo and the high silica group overlaps with generally higher pressures and temperature observed in Bromo when compared to the high silica group. Both groups follow similar trends in pressure and temperature as indicated in Fig. 4.2b.

In addition to clinopyroxene thermobarometry, orthopyroxene thermobarometry modelling (Putirka, 2008) was used to compare temperatures and pressures within the two groups that contained orthopyroxenes; Bromo and the high silica group. A test for equilibrium needed to be satisfied with a K_D (Fe-Mg) value of 0.29±0.06 between the orthopyroxene and groundmass of the samples. Samples from Bromo (T51) and the high silica group (T47) satisfied the test for equilibrium with the high silica group producing K_D (Fe-Mg) of 0.118-0.274 (n = 25) (outliers removed K_D = 0.237-0.274 (n = 23)) while Bromo (T51) ranged from 0.283-0.378 (n = 11) (if outliers removed 0.283-0.310 (n = 10)). Bromo (T52a) did not satisfy the test for equilibrium with K_D (Fe-Mg) values around 0.369 (n =2). This indicated that the orthopyroxene phase was not in equilibrium with the surrounding groundmass at the time of crystallisation.

The orthopyroxene and melt thermobarometry models of Putirka (2008) produced temperature estimates for the higher silica group of 996-1013°C (average = 1003°C, n = 23, σ = ±4.2°C) (Fig.4.2c). The pressure estimates from the orthopyroxene varied from 0.6-2.9 kbar (average = 2.0 kbar, n = 23, σ = ±0.6kbar). The orthopyroxene and groundmass from Bromo yielded temperatures of 1018-1037°C (average = 1026°C, n = 10, σ = ±5.5°C) while the pressure estimates ranged from 6.8-7.7 kbar (average = 7.4 kbar, n = 10, σ = ±0.27 kbar) (Fig.4.2c). Bromo and the high silica group show significant differences in crystallisation temperature and pressures despite being similar in major element geochemistry. Orthopyroxene in the high silica group crystallised at low temperature and pressure whereas the orthopyroxene in Bromo crystallised at relatively high temperature and pressure (Fig. 4.2c)..

4.1.2 Olivine-melt thermometry estimates

The olivine-melt thermometer models of Putirka (2008) were used to estimate the temperatures of olivine crystallisation in the Tengger Caldera Volcanic Complex. For accurate temperature estimates the olivine and glass composition need to satisfy a test for equilibrium with a K_D (Fe-Mg) value of 0.30±0.03.

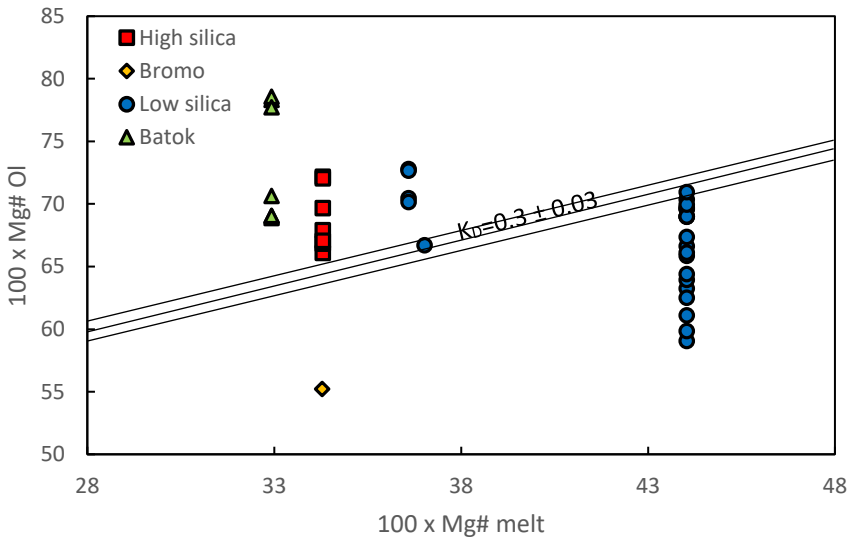

Figure 4.3: Test for equilibrium using K_D (Fe-Mg) between the olivine and glass groundmass of the respective sample close to the ideal of 0.30 from Putirka (2008).

It was found that only two olivine crystals from the low silica group satisfied equilibrium. T63 and T48 produced K_D (Fe-Mg) values of 0.293 and 0.322, respectively whilst the others yielded K_D (Fe-Mg) values of 0.13-0.55 (n = 40) (Fig.4.3). The temperatures from the thermometry for the two olivine crystals (from T63 and T48 respectively) were 1018°C and 949°C.

4.2 Depth of magma storage and crystallisation of Tengger Caldera Volcanic Complex

The pressure and temperature estimations were used to estimate the depths at which the mineral assemblages crystallised. These were translated into depths by using a rearranged version of $P = \rho g z$ (in where P=pressure; ρ = density of the Javanese crust: 2640kg/m^3; g = gravity constant 9.8m/s^2; z = depth) (Putirka, 2008). The density of the Javanese crust used for the estimation was obtained from Jeffery et al. (2013) inferred from crustal stratigraphy completed by Smyth et al. (2005, 2007).

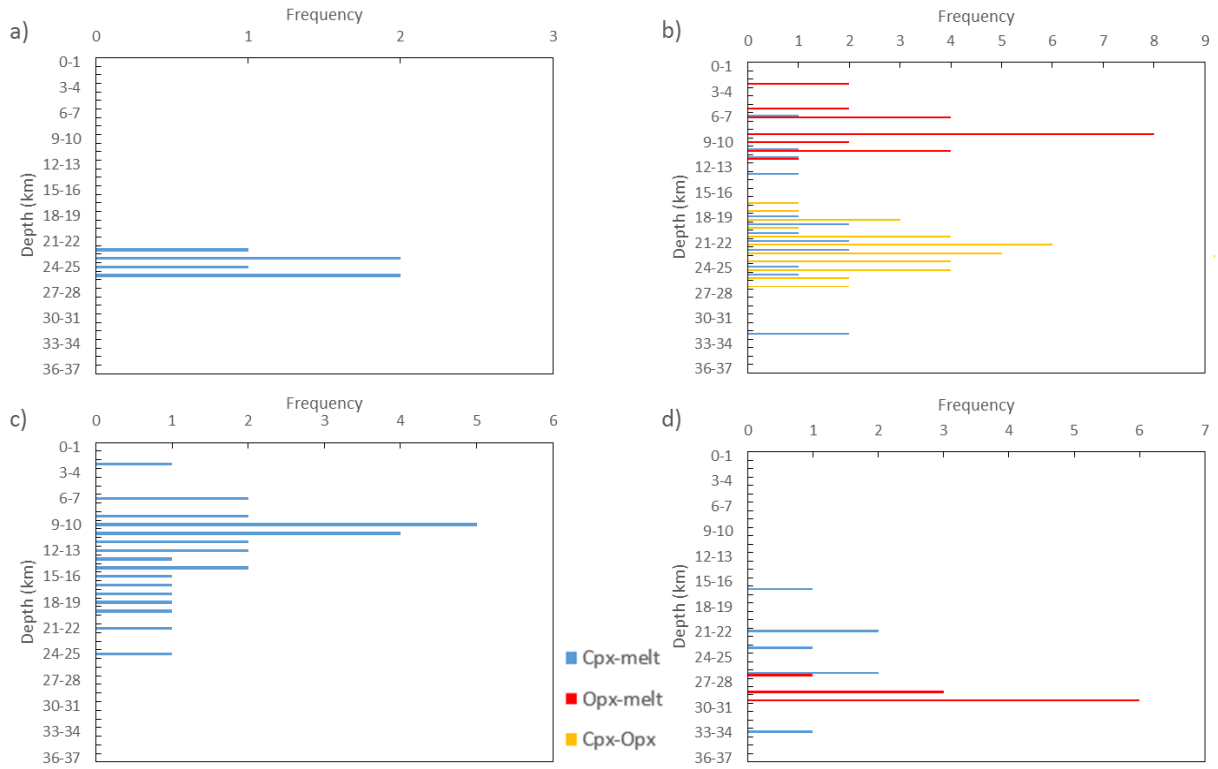

Figure 4.4: Frequency histograms from different thermobarometry models of different mineral assemblages by Putirka (2008) showing of number of analyses showing the most populated depth regions of the different groups observed in the Tengger-Bromo volcanic complex; a) Low silica group; b) high silica group; c) Batok and d) Bromo.

Clinopyroxene/melt and orthopyroxene/melt models produced the most consistent depth estimates. These suggested that the low silica group crystallised at depths of between 22 and 26 km (Fig.4.4a). In contrast, data from the high silica group indicates two regions of crystallisation, one at 7 to 11 km depth and another at 19-27 km that overlaps with the region inferred for the low silica group (Fig.4.4b). Batok produced relatively shallow depth estimates ranging from 7 to 13 km with material existing at deeper depths of up to 22 km. For Bromo, the depth estimates from clinopyroxene indicate 22 to 27 km whereas orthopyroxene suggest

29 to 30 km (Fig. 4.4d). Both Batok and the high silica group indicate a fairly shallow storage between ~7 and 12 km depths meanwhile both low silica, Bromo and the high silica groups indicate a deeper storage region between 20 and 28 km depth (Fig. 4.4). Bromo contains some orthopyroxenes that appear to have crystallised deeper at 29 to 30 km (fig.4.4). From the depth estimates it can be concluded that at least two definitive storage regions exist in the Tengger-Bromo Complex feeding the high silica group while Bromo is only fed by the deeper source and Batok is predominating fed by the upper source.

Multi-level storage systems are not uncommon in Java with multiple examples across the island from Merapi where there are multiple intertwined zones of crystallisation that are distributed between three reservoirs (Preece et al., 2014). These reservoirs occur at different depths; 30 km, 13 km and a more shallow zone <10 km deep where plagioclase, clinopyroxene and amphibole crystallise (Preece et al., 2014). A similar observation has been made for Krakatau (Dahren, 2018) and Kelut where mutli-level storage systems exist (Jeffery et al., 2013). Mapping of Bouguer anomalies in 1990s at the Tengger-Bromo complex and its surrounding region (Froger et al., 1992) indicated the calderas in the area were fed by at least two separate magma chambers. While one lies to the west of the complex the other major chamber occurs just to the north east in the Wontoro Valley which possibly could represent the magma storage facility feeding the Tengger-Bromo complex (Froger et al., 1992).

4.3 Magmatic processes and relationships within Tengger Caldera Volcanic Complex

The Tengger-Bromo volcanic complex contains a diverse array of magma groups that show an evolution over time in which chemically distinct magmas can be differentiated from one another. The high and low silica groups have separate chemical signatures revealed by comparing major and trace element concentrations that indicate unique processes affected magma generation beneath Tengger (Table 4.1). This chemical diversity in the two different silica group extends to the intra-caldera cones and Sandsea lava that exist in the Tengger Caldera Volcanic Complex. Large ion lithophile elements (LILE) have high concentrations and well defined trends such as observed for Ba (Ba = 400-1400 ppm) and Sr (Sr = 300-550) respectively (Fig.3.13f-g). The enrichment in Sr is seen exclusively in the low silica group and most likely reflects plagioclase and augite crystallisation. The high silica group has depletion in Sr, Ba and Sm.

Table 4.1: Geochemical signatures and intra-caldera volcanoes unique to the major silica groups observed at Tengger Caldera Volcanic Complex.

	Low silica group	High silica group
Samples associated	T25, T31, T32, T35, T43, T44, T45, T48, T59, T63	T12, T24*, T36, T37, T40, T47*, T55
Intra-caldera cones associated	Batok (T49,T50)	Bromo (T51, T52a, T52b) Sandsea (T15)
Unique geochemical signatures	Enrichment in Sr, Ba, Depletion in Hf, HFSE Tholeiitic	Enrichment in Hf, HFSE depletion in Ti, Sr, Ba, Sm and Eu Tholeiitic to transitional calc-alkaline Pigeonite and orthopyroxene
Depth of magma generation	Magma storage is more associated with deeper storage but Batok shows shallow storage as well.	Magma storage indicates both a deep and shallow storage region for magma

*= indicates the T47 and T24 which produce trace element signatures that are associated with the low silica group. T47 contains a high silica content but signatures consist of the low signature group

Although both systems produce tholeiitic magmas the two silica groups can also be determined in elements such as Zr, Y, Nd and Sm (Fig.3.12). When comparing Zr and Y, the two groups are distinct (except for T24 and T47 in some cases where they act as low silica group members) and in most cases indicate a cleat trend for the low silica group while the higher silica group are spread between tholeiitic and transitional calc-alkaline magmas (Fig.3.10). Figure 4.5 highlights that this trend in ternary diagram form shows that the majority of the samples are tholeiitic and follow the general curve observed in volcanic rocks from Java. The groups are thought to be a result of early crystallisation of magnetite within the magma which would result in the low Fe_2O_3 that is observed in the high silica rocks (Fig. 4.5). The high silica group (and Bromo) contain titanomagnetite in low quantities in the groundmass, yet it is more prevalent as inclusions within the plagioclase phenocrysts. Similar observations have been made for the lower silica group, although the high silica group are the only lavas to contain orthopyroxene and pigeonite.

The geochemical trends of the different groups can be used to differentiate between the magma mixing and crystal fractionation. The major element concentrations of many elements such as Al_2O_3, MgO, CaO form linear trends which are usually consistent with a magma mixing as the system evolves from low to high silica lavas (Fig.3.11). However Fe_2O_3 and TiO_2 from two different trends. Fe_2O_3 produces two linear negative trends both negative indicating that it is behaving compatibly however the two trends have for the high and low silica groupings. This indicates that the mixing is not the only main process at play at Tengger.

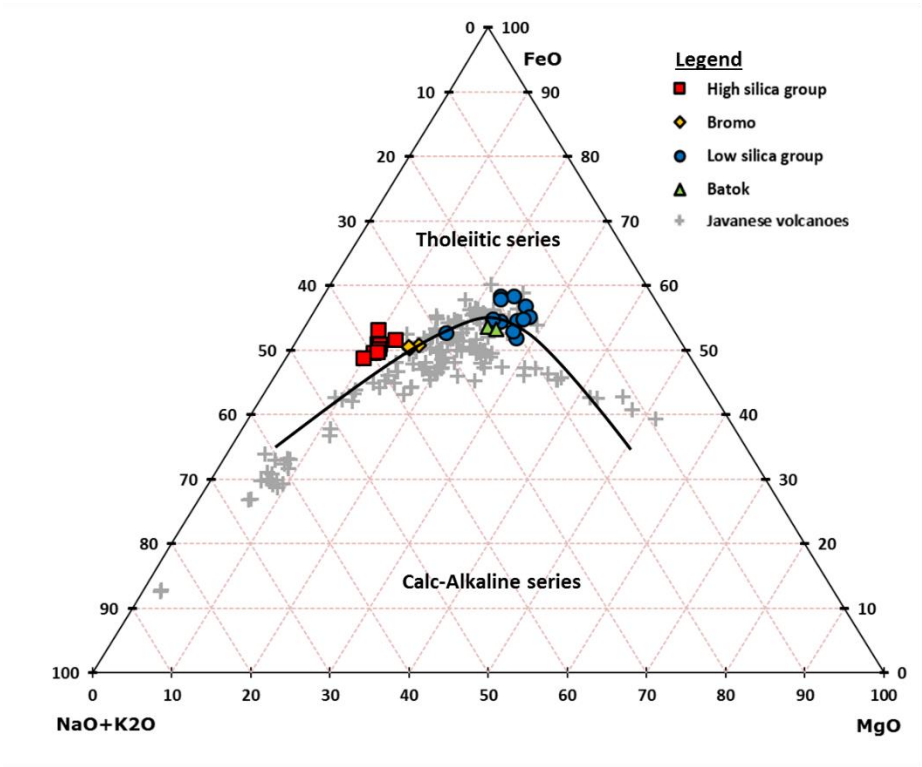

Figure 4.5: AFM diagram distinguishing tholeiitic and calc-alkaline series of the four groups of lavas found at Tengger Caldera Volcanic Complex compared to regional volcanism in Java. Data from Salak (Handley et al.,2008), Gede (Handley et al., 2010), Papandayan (Whitford, 1975; Whitford et al., 1981; White and Patchett,1984; Woodhead et al., 2001), Guntur (Edwards, 1990); Galunggung (Whitford, 1975; Gerbe et al., 1992; Turner and Foden, 2001), Cereme (Edwards, 1990), Slamet (Vukadinovic and Sutawidjaja, 1995), Sumbing (Whitford, 1975; Woodhead et al., 2001), Ungaran (Whitford, 1975; Claproth, 1989, Woodhead et al., 2001), Merbabu (Gertisser, unpublished), Merapi (Woodhead et al., 2001; Troll et al., 2013; Handley et al., 2014), Kelut (Jeffery et al., 2013), Semeru (Whitford, 1975; Carn and Pyle, 2001; Woodhead et al., 2001), Lamongan (Whitford, 1975; Carn and Pyle, 2001; Woodhead et al., 2001) and Ijen (Handley et al., 2007).

It is thought fractional crystallisation is responsible for the trends observed in Fe_2O_3 and TiO_2. In the case of the high silica group the trends are thought to be related to the early crystallisation of titanomagnetite and the formation of pigeonite and orthopyroxene consistent with in the observed mineralogy (Table 4.1). This caused the change of Fe_2O_3 trend compared to the low silica group which crystallises only low amounts of orthopyroxene (Fig.3.11). This is reflected in the trace element chemistry where similar trends are observed in Hf and Sr (Fig.3.12). It is postulated that both fractional crystallisation and magma mixing play both an important role differentiating the two silica groups that exist within the Tengger-Bromo volcanic complex.

4.4 Spatial and temporal relationships within Tengger Caldera Volcanic Complex

The region in which the Tengger Caldera Volcanic Complex sits first experienced volcanism around 820,000 years ago according to studies by Mulyadi (1992) and Van Gerven and Pichler (1995). From the stratigraphy and depth estimates a basic petrogenetic model is postulated in which the original magma storage unit was stored deeper at 22 and 26km with the initial lava erupting to form the Tengger volcano seen at the base of the caldera wall (Fig.4.6a) up to 265,000 years ago (Van Gerven and Pichler, 1995).

This initial phase of eruption was dominated by basaltic lavas of the low silica group. Based on the stratigraphy this sequence was terminated by the caldera forming sequence which Van Gerven and Pichler (1995) indicate occurred over 45000 years ago. This is evident in the caldera wall by the initiation of a sequence of ignimbrite deposits comprised of lava spatter and bedded lapilli all belonging to the low silica group. This sequence exhibits a range of compositions from basalt to basaltic andesite with the outlier T47 being andesitic in composition. The depth estimates suggest that the tholeiitic magma originated from the deeper storage region around 22 and 26km. This sequence initiated the formation of the caldera itself with much of the material forming the north western wall and the lower units of then north eastern wall (Van Gerven and Pichler, 1995). This sequence is capped by an ignimbrite which produced the low silica lava before the system moved into a sequence of high silica volcanism.

The sequences above the first caldera-forming sequence are defined by their silica content with high silica lavas making up most of the sequence. The units within the sequence are mostly bedded lapilli and interbedded ash which represent part of a period dominated by intermittent breaks and changes in eruption style which make up the second stage of formation. The lavas from this unit originate from a shallow storage region. The silica content within these lavas is constant for most of the sequence but towards the top of the sequence the silica content of the lava sharply transitions back to the low silica group indicating a change of source back to the original silica group that initiated volcanism. Many of the rocks from this sequence are compositionally similar to a trachy-andesite.

The uppermost section of the caldera rim is dominated by the post caldera sequence that contains a mixture of high and low silica lavas. The post caldera sequence is most likely related to the intracaldera volcanism of the now truncated cones. This indicates it may be comprised

of material erupted from either Bromo or Batok which was deposited on the upper caldera wall, hence the alternating change of silica content and geochemical signatures. Additionally the different geochemical groups indicate that different storage regions erupted lavas at different stages during this sequence. This sequence produced varied compositions ranging from basaltic andesite to trachy-andesite.

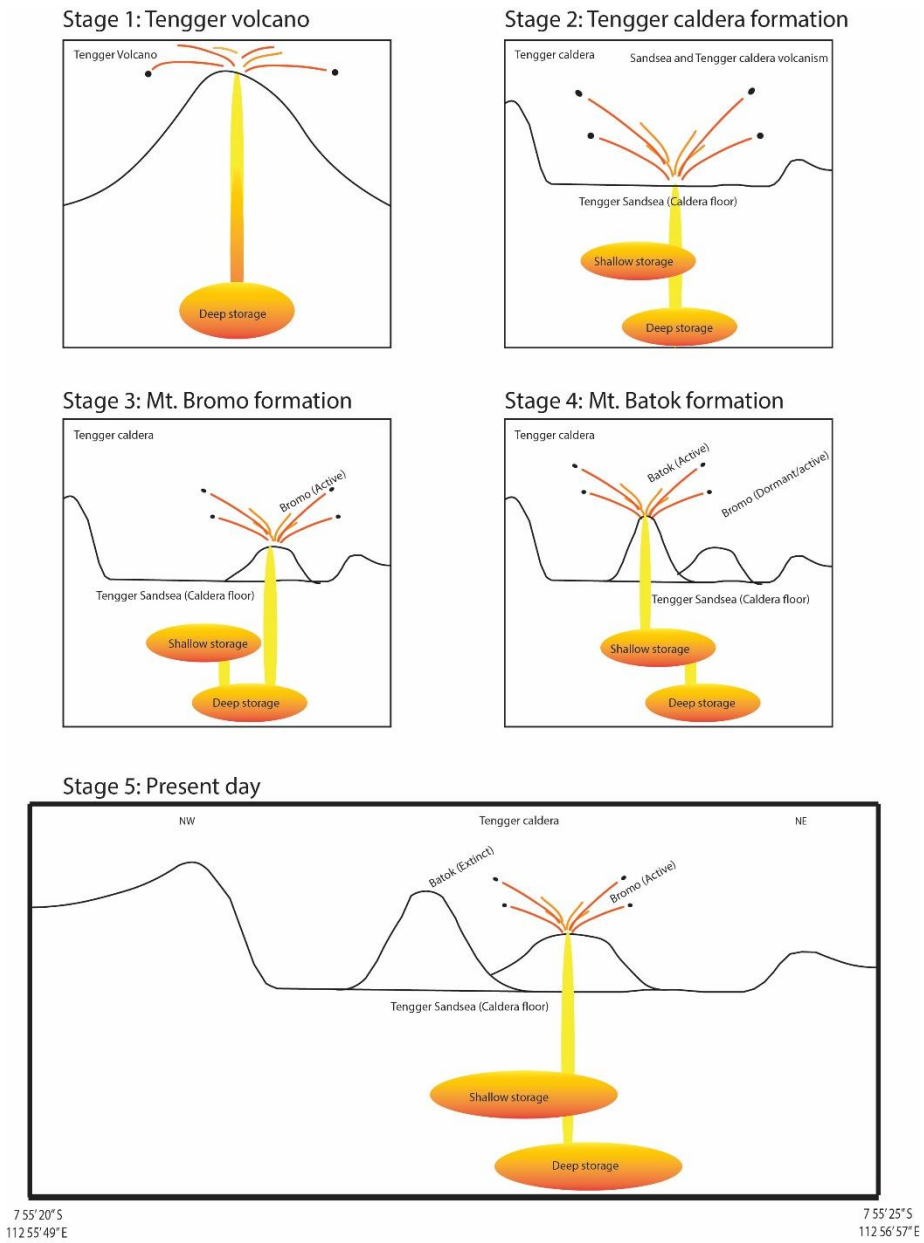

Figure 4.6: The general evolution of the Tengger-Bromo Volcanic complex showing eruption stages over time.

From stage 3 to present, much of the volcanic activity and resultant deposits have been dominated by the intracaldera centres of Bromo and Batok. Van Gerven and Pichler (1995) state that activity at Bromo started then stopped (Stage 3), then activity shifted to Batok (Stage

4) prior to shifting back to Bromo again in more recent times. The cone Batok produced eruptions of low silica lava from a relatively shallow depths (Smithsonian, 2017). This in turn produce the well-formed cinder cone observed today and the basaltic andesite commonly associated with this cone. Additionally the source was geochemically distinct to, and closely resembled those associated with the low silica group. Batok lavas similar temperatures across a significant range in pressure indicating that crystallisation occurred at different depths prior to eruption. This may indicate rapid magma ascent (little time to cool upon ascent). The multiple staged storage suggested for the TCVC is not uncommon at Sunda arc volcanoes with volcanoes such as Merapi, Krakatau and Kelut showing multiple levels of magmatic storage and crystallisation (Dahren, 2018; Preece et al., 2014; Jeffery et al., 2013).

Batok's volcanism was terminated by the restart of volcanism at Bromo which reverted to the high silica lavas commonly observed in the high silica groups. The depth estimates indicated that the magma originating from the deeper storage region. Currently Bromo is the only active cone within the TCVC intermittently erupting gas and ash that has been deposited on the surrounding Sandsea and caldera walls.

4.5 Regional geochemical and tectonic comparison

When placed in a regional context, the Tengger Caldera Volcanic Complex produces distinctive geochemical trends in major and trace elements in contrast with the surrounding volcanoes (such as Kelut, Willis and Lawu). Semeru, a stratovolcano to the south of Tengger produces a similar trend in total alkalis versus silica. The lavas erupted from Tengger are found to be potassic tholeiitic magmas which closely relate geochemically to Lamongan lavas as both trend to high concentrations of Ba as the magmas evolve (Whitford, 1975; Carn and Pyle, 2001; Woodhead et al., 2001). The volcanic rocks from TCVC show some of the highest Ba concentrations in Javanese rocks so far analysed. At Salak, a volcano with similarly high Ba concentrations, similar correlations are observed in the lavas when comparing TiO_2, P_2O_5 and Y (Handley et al., 2008). The alkali content of Tengger lavas do not follow the common trends of other East Javanese volcanoes within the region (Fig. 4.7). The trends produced steep positive correlations when comparing total alkalis versus silica. Overall the Tengger Caldera Volcanic Complex produces a chemically unique suite of lavas that do not conform to the common trends observed over the Sunda Arc in general and only produces similarities among a few volcanoes across the island of Java.

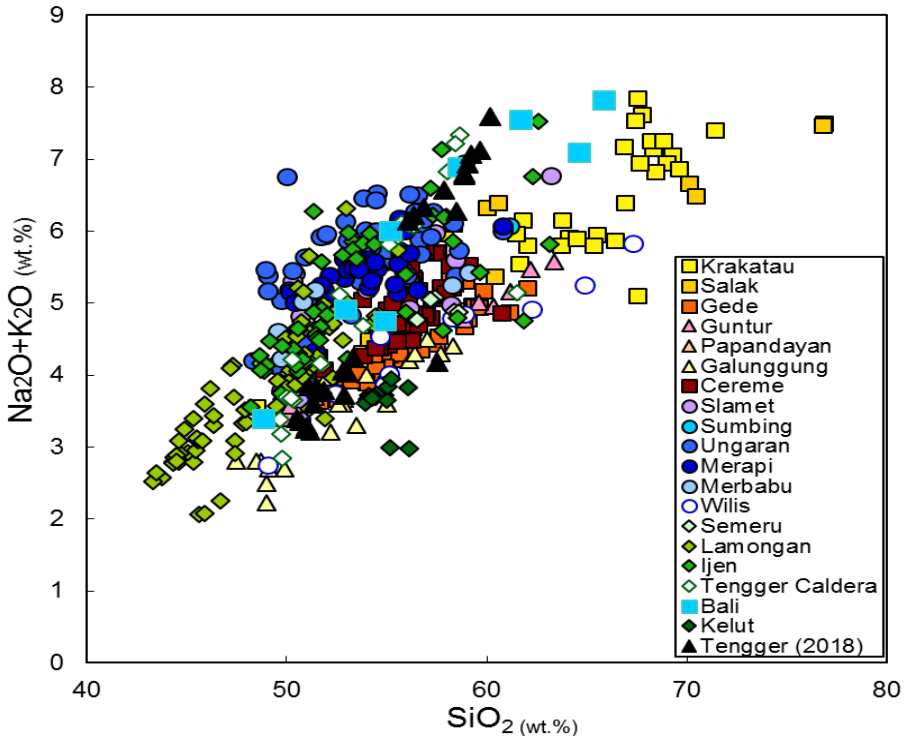

Figure 4.7: Total alkalis versus silica diagram of bulk rock compositions of Javanese volcanoes for comparison to new data from Tengger Caldera. West Java shown in squares, Central Java shown as circles, and East Java as triangles. Data from Salak (Handley et al.,2008), Gede (Handley et al., 2010), Papandayan (Whitford, 1975; Whitford et al., 1981; White and Patchett,1984; Woodhead et al., 2001), Guntur (Edwards, 1990); Galunggung (Whitford, 1975; Gerbe et al., 1992; Turner and Foden, 2001), Cereme (Edwards, 1990), Slamet (Vukadinovic and Sutawidjaja, 1995), Sumbing (Whitford, 1975; Woodhead et al., 2001), Ungaran (Whitford, 1975; Claproth, 1989, Woodhead et al., 2001), Merbabu (Gertisser, unpublished), Merapi (Woodhead et al., 2001; Troll et al., 2013; Handley et al., 2014), Kelut (Jeffery et al., 2013), Semeru (Whitford, 1975; Carn and Pyle, 2001; Woodhead et al., 2001), Lamongan (Whitford, 1975; Carn and Pyle, 2001; Woodhead et al., 2001) and Ijen (Handley et al., 2007).

Chapter 5: Conclusions and future work

This study set out to expand on the limited research so far conducted on the Tengger Caldera Volcanic Complex by investigating the volcanic deposit characteristics (grain-size, texture, colour etc.) to develop an overall volcanic stratigraphy of the Tengger Caldera Volcanic Complex between the different phases and eruption sequences. Insight into the petrology and geochemical trends allowed a greater understanding of the relationships that exist in the TCVC and the intracaldera cones within it. Geochemically constrained groups were established and linked to the stratigraphy to understand the evolution of the magmas over time. Mineralogy provided constraints on the storage systems that are play underneath Tengger with the geochemical groups indicating the unique signatures that exist beneath the volcano. Several conclusions can be made on the Tengger Caldera Volcanic Complex:

- Three main eruptive stages are observed which can be divided into 6 sequences within the stratigraphy of the TCVC. These include pre-caldera, caldera forming (1), caldera forming (2), post caldera, intracaldera (Batok and Bromo) and the outer caldera flank sequences.
- The geochemistry identified two distinct geochemical groups observed in TCVC which include the high and low silica groups with two intracaldera associated with the groups; Batok and Bromo. Each of the groups produced distinct different geochemical signatures when compared to N-MORB in addition to producing different trends within both major and trace element analysis. The TCVC are tholeiitic to calc-alkaline in nature. Bromo samples contain phenocrysts of pigeonite, which is absent elsewhere in the system
- Depth estimates indicate two major storage regions that exist beneath Tengger with a shallow region at 7 to 11 km and a deeper region at 19 to 27 km. The deeper storage region was found to feed the high silica group and Bromo and while the shallow storage fed the low and high silica group. Batok was fed by a shallower source compared to Bromo.
- TCVC produces a chemically unique suite of lavas that do not conform to the common trends observed in East Javanese volcanoes and only produces similarities among a few volcanoes across the island of Java such as the Lamongan lavas.

The work that was undertaken focused primarily on the geochemical trends within the lavas and tephra of the Tengger caldera and its associated cones. However much remains unknown about the complex itself and hence future work is needed to fully understand the mechanisms at play beneath the Tengger Caldera Volcanic Complex. Suggested areas of future work include:

Effective dating of the stratigraphy on the North West and Eastern walls either by K-Ar or radiocarbon dating. The possibility of using charcoal obtained from the one layer in the North Eastern caldera wall could be used to obtain good radiocarbon ages in relation to the surrounding layers. In addition further field is required to obtain samples of any other charcoal layers that may beneficial to the study.

Further sampling from the other intracaldera cones that make up the internal complex of Tengger in order to identify their spatial and temporal relationships within the system and if they correlate with the magmas obtained from this study. This would include further mapping to understand the structure of the caldera and the complexes that exist around Tengger.

Isotope geochemistry (such as O, Sr, Nd, Hf and Pb) could be used to identify to source material and to further constrain magmatic differentiation, input of crustal material, assimilation and or contamination. A possible geophysical study using different geophysical techniques to distinguish underlying structures such as the storage region and feeder systems that power Tengger as well as correlating back to the results obtained by Van Gerven and Pichler (1995).

References

Abdullah, C. I., Rampnoux, J. P., Bellon, H., Maury, R. C., and Soeria-Atmadja, R. (2000). The evolution of Sumba Island (Indonesia) revisited in the light of new data on the geochronology and geochemistry of the magmatic rocks. Journal of Asian Earth Sciences, 18, 533-546.

Aiuppa, A., Bani, P., Moussallam, Y., Di Napoli, R., Allard, P., Gunawan, H., and Tamburello, G. (2015). First determination of magma-derived gas emissions from Bromo volcano, eastern Java (Indonesia). Journal of Volcanology and Geothermal Research, 304, 206-213.

Carn, S.A., and Pyle, D.M. (2001). Petrology and geochemistry of the Lamongan Volcanic Field, East Java, Indonesia: Primitive Sunda Arc magmas in an extensional tectonic setting? Journal of Petrology. 42. 1643-1683.

Chadwick J. P., Troll V. R., Ginibre C., Morgan D., Gertisser R., Waight T. E. and Davidson J. P. (2007) Carbonate assimilation at Merapi Volcano, Java, Indonesia: insights from crystal isotope stratigraphy. Journal of Petrology. 48, 1793–1812.

Claproth, R. (1989). Petrography and geochemistry of volcanic rocks from Ungaran, Central Java, Indonesia. Unpublished PhD thesis, Department of Geology, University of Wollongong, Australia.

Clements, B., Hall, R., Smyth, H. R., and Cottam, M. A. (2009). Thrusting of a volcanic arc: a new structural model for Java. Petroleum Geoscience, 15, 159-174.

Dahren, B. (2018). Investigating Magma Plumbing Beneath Anak Krakatau Volcano, Indonesia: Evidence for Multiple Magma Storage Regions. Contributions to Mineralogy and Petrology 163, 631-651.

Davidson, J. P., Hora, J. M., Garrison, J. M., and Dungan, M. A. (2005). Crustal forensics in arc magmas. Journal of Volcanology and Geothermal Research, 140, 157-170.

Demets, C., Gordon, R. G., Argus, D. F., and Stein, S. (1990). Current Plate Motions. Geophysical Journal International, 101, 425-478.

Dungan, M.A., Wulff, A., and Thompson, R., 2001. Eruptive stratigraphy of the Tatara–San Pedro Complex 368S, Southern Volcanic Zone, Chilean Andes: reconstruction method and implications for magma evolution at long-lived arc volcanic centers. Journal of Petrology. 42, 555– 626.

Edwards, C.M.H. (1990). Petrogenesis of tholeiitic, calcalkaline and alkaline volcanic rocks, Sunda arc, Indonesia. Ph.D. Thesis, Royal Holloway, University of London.

Fiantis, D., Nelson, M., Shamshuddin, J., & Van Ranst, L. E. (2010). Determination of the geochemical weathering indices and trace elements content of new volcanic ash deposits from Mt. Talang (West Sumatra) Indonesia. Eurasian Soil Science, 43, 1477–1485.

Firth, C.W., Handley, H.K., Turner, S.P., Cronin, S.J., Smith, I.E. (2016). Variable conditions of magma storage and differentiation with links to eruption style at Ambrym Volcano, Vanuatu. Journal of Petrology 57, 1049-1072.

Froger, J. L., Bonneville, A., and Mulyadi, E. (1992). Gravimetric Signature of Calderas and Magma Chambers - Example of Tengger Volcano (East Java). Comptes Rendus De L Academie Des Sciences de Paris Serie II, 315, 749-755.

Gasparon M. and Varne R. (1998) Crustal assimilation versus subducted sediment input in west Sunda arc volcanics: an evaluation. Mineral. Petrol. 64, 89–117.

Genevraye, P. D., and Samuel, L. (1972). Geology of the Kendeng Zone (Central and East Java). Paper presented at the Proceedings Indonesian Petroleum Association 1st Annual Convention, Proceedings, 17-30.

Gertisser, R. & Keller, J. (2003).Trace element and Sr, Nd, Pb and O isotope variations in medium-K and high-K volcanic rocks from Merapi Volcano, Central Java, Indonesia: evidence for the involvement of subducted sediments in Sunda Arc magma genesis. Journal of Petrology 44, 457-489.

Gottschammer, E., & Surono, I. (2000). Locating tremor and shock sources recorded at Bromo Volcano. Journal of Volcanology and Geothermal Research, 101, 199-209.

Hall, R. (2011). Australia-SE Asia collision: plate tectonics and crustal flow. Se Asian Gateway: History and Tectonics of the Australia-Asia Collision, 355, 75-109.

Hall, R., and Sevastjanova, I. (2012). Australian crust in Indonesia. Australian Journal of Earth Sciences, 59, 827-844.

Hall, R., and Smyth, H. R. (2008). Cenozoic arc processes in Indonesia: Identification of the key influences on the stratigraphic record in active volcanic arcs. Formation and Applications of the Sedimentary Record in Arc Collision Zones, 436, 27-54.

Hall, R., and Spakman, W. (2002). Subducted slabs beneath the eastern Indonesia-Tonga region: insights from tomography. Earth and Planetary Science Letters, 201, 321-336.

Hamilton, W. B. (1979). Tectonics of the Indonesian region. U.S. Geological Survey Professional Paper reprinted with corrections, 1985 and 1985, 1078.

Handley, H. K., Blichert-Toft, J., Gertisser, R., Macpherson, C. G., Turner, S. P., Zaennudin, A., and Abdurrachman, M. (2014). Insights from Pb and O isotopes into along-arc variations in subduction inputs and crustal assimilation for volcanic rocks in Java, Sunda arc, Indonesia. Geochimica et Cosmochimica Acta, 139, 205-226.

Handley, H. K., Davidson, J. P., Macpherson, C. G., and Stimac, J. A. (2008). Untangling differentiation in arc lavas: Constraints from unusual minor and trace element variations at Salak Volcano, Indonesia. Chemical Geology, 255, 360-376.

Handley, H. K., Macpherson, C. G., and Davidson, J. P. (2010). Geochemical and Sr-O isotopic constraints on magmatic differentiation at Gede Volcanic Complex, West Java, Indonesia. Contributions to Mineralogy and Petrology, 159, 885-908.

Handley, H. K., Macpherson, C. G., Davidson, J. P., Berlo, K., and Lowry, D. (2007). Constraining fluid and sediment contributions to subduction-related magmatism in Indonesia: Ijen Volcanic Complex. Journal of Petrology, 48, 1155-1183.

Handley, H. K., Macpherson, C. G., Davidson, J. P., and Gertisser, R. (2006). Along-arc heterogeneity in crustal architecture and subduction input at the Sunda arc in Java, Indonesia. Geochimica Et Cosmochimica Acta, 70, A227-A227.

Hildreth W, Moorbath S (1988) Crustal contributions to arc magmatism in the Andes of Central Chile. Contributions Mineral Petrology 98:455–489.

Hutchison C. S. (1975) Ophiolite in Southeast Asia. Geol. Soc. Am. Bull. 86, 797–806.

Jeffery, A. J., Gertisser, R., Troll, V. R., Jolis, E. M., Dahren, B., Harris, C., and Chadwick, J. P. (2013). The pre-eruptive magma plumbing system of the 2007-2008 dome-forming eruption of Kelut volcano, East Java, Indonesia. Contributions to Mineralogy and Petrology, 166, 275-308.

Katili, J. A. (1975). Volcanism and plate tectonics in the Indonesian island arcs. Tectonophysics, 26, 165-188.

Kopp, H., Flueh, E. R., Petersen, C. J., Weinrebe, W., Wittwer, A., and Scientists, M. (2006). The Java margin revisited: Evidence for subduction erosion off Java. Earth and Planetary Science Letters, 242, 130-142.

Le Pichon, X. (1968). Sea-floor spreading and continental drift. Journal of Geophysical Research, 73, 3661-3697.

MacLean, W.H., Barrett, T.J., 1993. Lithochemical techniques using immobile elements. Journal of Geochemical Exploration. 48, 109–133.

Mandeville, C. W., Carey, S., and Sigurdsson, H. (1996). Magma mixing, fractional crystallization and volatile degassing during the 1883 eruption of Krakatau volcano, Indonesia. Journal of Volcanology and Geothermal Research, 74, 243-274.

McDonough, W., and Sun, S. (1995). Composition of the Earth. Chemical Geology. Vol 120, 223-253.

Metcalfe I. (1990) Allochthonous terrane processes in Southeast Asia. Philosophical Transactions of the Royal Society, London. A331, 625–640.

Miyashiro, A. (1974).Volcanic Rock Series and Tectonic Setting. Annual Review of Earth and Planetary Sciences, Vol. 3, 251.

Mulyadi, E. (1992). Le complexe de Bromo-Tengger (East Java, Indonesie). Etude structurale et volcanologique. Available from http://www.theses.fr/1992CLF21453

Newhall, C., and Dzurisin, D. (1989). Historical unrest at large calderas of the world. U.S. Geological Survey Bulletin 18558, 1108.

Pacey, A., Macpherson, C. G., and McCaffrey, K. J. W. (2013). Linear volcanic segments in the central Sunda Arc, Indonesia, identified using Hough Transform analysis: Implications for arc lithosphere control upon volcano distribution. Earth and Planetary Science Letters, 369, 24-33.

Plank, T., Kelley, K. A., Zimmer, M. M., Hauri, E. H., and Wallace, P. J. (2013). Why do mafic arc magmas contain similar to 4 wt% water on average? Earth and Planetary Science Letters, 364, 168-179.

Preece, K., Gertisser, R., Barclay, J., Berlo, K., Herd, R. A., and Edinburgh Ion Microprobe Facility. (2014). Pre- and syn-eruptive degassing and crystallisation processes of the 2010 and 2006 eruptions of Merapi volcano, Indonesia. Contributions to Mineralogy and Petrology, 168, 1061.

Price, R.C., Stewart, R.B., Woodhead, J.D., Smith, I.E.M., 1999. Petrogenesis of high-K Arc magmas: evidence from Egmont Volcano, North Island, New Zealand. Journal of Petrology. 40, 167– 197.

Putirka, K. D. (2008). Thermometers and Barometers for Volcanic Systems. In Putirka, K. D. (Ed) Minerals, Inclusions and Volcanic Processes, 69, 61-120. Reviews in Mineralogy, 69, 61-120.

Reubi, O., and Nicholls, I. A. (2004). Magmatic evolution at Batur volcanic field, Bali, Indonesia: petrological evidence for polybaric fractional crystallization and implications for caldera-forming eruptions. Journal of Volcanology and Geothermal Research, 138, 345-369.

Simandjuntak, T. O., and Barber, A. J. (1996). Contrasting tectonic styles in the Neogene orogenic belts of Indonesia. Geological Society, London, Special Publications, 106, 185-201.

Smithsonian. (2017). Tengger Caldera. Retrieved from: https://volcano.si.edu/volcano.cfm?vn=263310

Smyth, H. R., Hall, R., Hamilton, J., and Kinny, P. D. (2005). East Java: Cenozoic Basins, volcanoes and ancient basements. Proceedings, Indonesian Petroleum Association, 13th Annual Convention and Exhibition, August 2005, 251-266.

Smyth, H. R., Hall, R., and Nichols, G. J. (2008). Cenozoic volcanic arc history of East Java, Indonesia: The stratigraphic record of eruptions on an active continental margin. Formation and Applications of the Sedimentary Record in Arc Collision Zones, Geological Society of American Special Paper, 436, 199-222.

Soeria-Atmadja, R., Maury, R. C., Bellon, H., Pringgoprawiro, H., Polve, M., and Priadi, B. (1994). Tertiary magmatic belts in Java. Journal of Southeast Asian Earth Sciences, 9, 13-27.

Solikhin, A., Thouret, J. C., Gupta, A., Harris, A. J. L., and Liew, S. C. (2012). Geology, tectonics, and the 2002-2003 eruption of the Semeru volcano, Indonesia: Interpreted from high-spatial resolution satellite imagery. Geomorphology, 138, 364-379.

Syracuse, E. M., and Abers, G. A. (2006). Global compilation of variations in slab depth beneath arc volcanoes and implications. Geochemistry Geophysics Geosystems, 7.

Tepley FJ III, Davidson JP, Tilling RI, Arth JG (2000) Magma mixing, recharge and eruption histories recorded in plagioclase phenocrysts from El Chichon, Mexico. Journal of Petrology, 41, 1397–1411.

Thirlwall, M. F., Graham, A. M., Arculus, R. J., Harmon, R. S., and Macpherson, C. G. (1996). Resolution of the effects of crustal assimilation, sediment subduction, and fluid transport in island arc magmas: Pb-Sr-Nd-O isotope geochemistry of Grenada, Lesser Antilles. Geochimica et Cosmochimica Acta, 60, 4785-4810.

Tregoning, P., Brunner, F. K., Bock, Y., Puntodewo, S. S. O., Mccaffrey, R., Genrich, J. F., and Subarya, C. (1994). 1st Geodetic Measurement of Convergence across the Java Trench. Geophysical Research Letters, 21, 2135-2138.

Troll V. R., Deegan F. M., Jolis E. M., Harris C., Chadwick J. P., Gertisser R., Schwarzkopf L. M., Borisova A. Y., Bindeman I. N., Sumarti S. and Preece K. (2013) Magmatic differentiation processes at Merapi Volcano: inclusion petrology and oxygen isotopes. Journal of Volcanology and Geothermal Research, 261, 38–49.

Turner, S., and Foden, J. (2001). U, Th, and Ra disequilibria, Sr, Nd and Pb isotope and trace element variations in Sunda arc lavas: predominance of a subducted sediment component. Contributions of Mineralogy and Petrology, 142, 43-57.

Van Gerven, M., and Pichler, H. (1995). Some Aspects of the Volcanology and Geochemistry of the Tengger Caldera, Java, Indonesia - Eruption of a K-Rich Tholeiitic Series. Journal of Southeast Asian Earth Sciences, 11, 125-133.

Wheller, G. E., Varne, R., Foden, J. D., and Abbott, M. J. (1987). Geochemistry of Quaternary Volcanism in the Sunda-Banda Arc, Indonesia, and 3-Component Genesis of Island-Arc Basaltic Magmas. Journal of Volcanology and Geothermal Research, 32, 137-160.

White, W.M., and Patchett, J. (1984). Hf-Nd-Sr isotopes and incompatible element abundances in island arcs: implications for magma origins and crustal-mantle evolution. Earth and Planetary Science Letters, 67, 167-185.

Whitford D. J. (1975) Strontium isotopic studies of the volcanic rocks of the Sunda arc, Indonesia, and their petrogenesis. Geochimica et Cosmochimica Acta, 39, 1287–1302.

Whitford D. J. and Nicholls I. A. (1976) Potassium variations in lavas across the Sunda arc in Java and Bali. In R. W. Johnson Volcanism in Australasia. Elsevier, Amsterdam, 63–75.

Whitford, D. J., Nicholls, I. A., and Taylor, S. R. (1979). Spatial Variations in the Geochemistry of Quaternary Lavas Across the Sunda Arc in Java and Bali. Contributions to Mineralogy and Petrology, 70, 341-356.

Whitford, D.J., White, W.M. and Jezek, P.A (1981). Neodymium isotopic composition of Quaternary island arc lavas from Indonesia. Geochemica et Cosmochimica Acta, 45, 989-995.

Woodhead, J.D., Hergt, J.M., Davidson, J.P and Eggins, S.M. (2001). Hafnium isotope evidence for ‘conservative’ element mobility during subduction processes. Earth and Planetary Science Letters, 192, 331-346.

Vukadinovic, D., and Sutawidjaja, I. (1995). Geology, mineralogy and magma evolution of Gunung Slamet Volcano, Java, Indonesia. Journal of Southeast Asian Earth Sciences, 11, 135-164.

Appendix

Table A.1: Main texture descriptions and classification of Plagioclase phenocrysts.

Type	1	2	3	4
Textural description	Euhedral to subhedral crystals seen throughout the samples with many containing sieve type texture throughout entire crystals. Other crystals contain weathering with sericite occurring in fractures of crystal. Inclusions and weathering observed and clustering in some samples. Lamellar twinning commonly observed	Subhedral single phenocrysts with significant chemical variation observed. Inclusion sometimes seen. Carlsbad twinning rarely observed with lamellar twinning most common. Zonation not as clear as other types but observed in the largest crystals. Sieve texture sometimes observed.	Most common zoned crystal observed mostly seen as subhedral phenocrysts either single or clustered. Inclusion observed inside or in spaces between crystals. Slight chemical variation observed from core to rim. Sometimes fractured and weathered. Sieve texture sometimes observed in core of crystal. Lamellar twinning commonly observed.	Fairly subhedral crystals with some observed as euhedral shape. Reaction rims define this type with it commonly observed. Addition inclusion prevalent throughout and observed fractures. Chemical variation observed from inner crystal core and outer boundary rims where reaction rim occurs. Lamellar twinning observed in most crystals.
Zonation	No zonation	Normal or reversed zonation	Concentric zoning comprised of normal and reverse zoning	Slight normal and reverse zonation observed
Inclusions	Melt; titanomagnetite; sometimes Ol, Opx and Cpx	Melt; titanomagnetite; sometimes Ol, Opx and Cpx	Melt; titanomagnetite; sometimes Ol, Opx and Cpx	Melt; titanomagnetite; sometimes Ol, Opx and Cpx
Size	100-1000µm	250-4000µm	600-5000µm	250-900µm
Photo	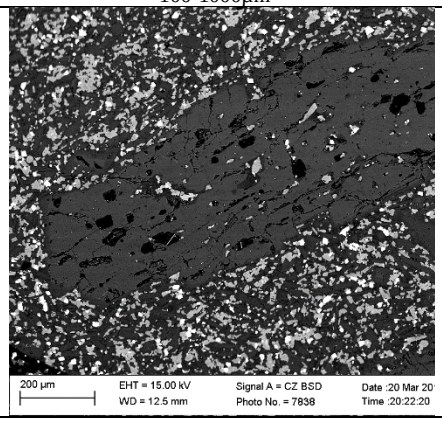	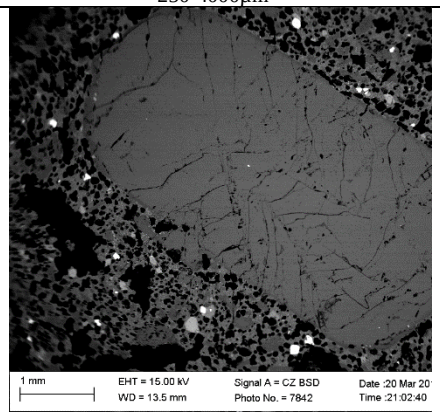	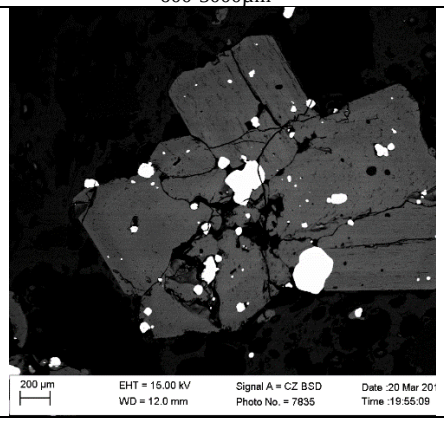	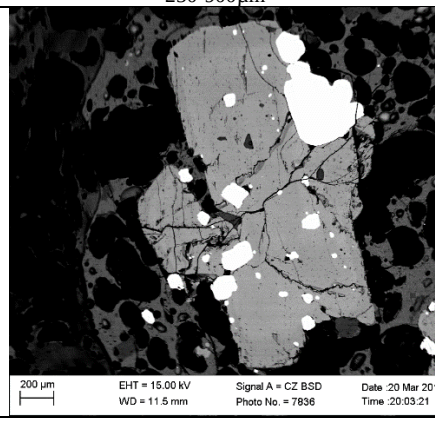

Note each photo scale differs. Descriptions include texture type, comments, zoning patterns, inclusions and Size ranges (>300 µm phenocrysts; 300-100 µm microcrysts; <100 µm microlites). Photomicrographs of each texture taken on a ZEISS Scanning Electron Microscope. Type sample T48; type 2 sample T49; type 3 sample T47; type 4 sample T47

Table A.2: Main texture descriptions and classification of Clinopyroxene phenocrysts.

Type	**1**	**2**	**3**
Textural description	Single twinned phenocrysts. Very little chemical variation observed in crystal though inclusions sometimes seen. Fracturing seen in some crystals and sometimes clustered with orthopyroxene, plagioclase and oxide crystals.	Euhedral to subhedral single phenocrysts observed usually twinned. Most contain inclusions with faint chemical variation observed. Rarely is seen to have sieve texture in crystal.	Usually occurs as small phenocrysts with small inclusions. Forms usually subhedral crystal shapes and often fairly weathered. Sometimes fractured.
Zonation	No zonation	Concentric zoning comprised of normal and reverse zoning	Faintly zoned either normal or reverse zoning
Inclusions	Melt; titanomagnetite; sometimes plag, opx and cpx	Melt; titanomagnetite; sometimes plag, opx and cpx	Melt; titanomagnetite
Size	250-1100µm	500-1100µm	250-900µm
Photo	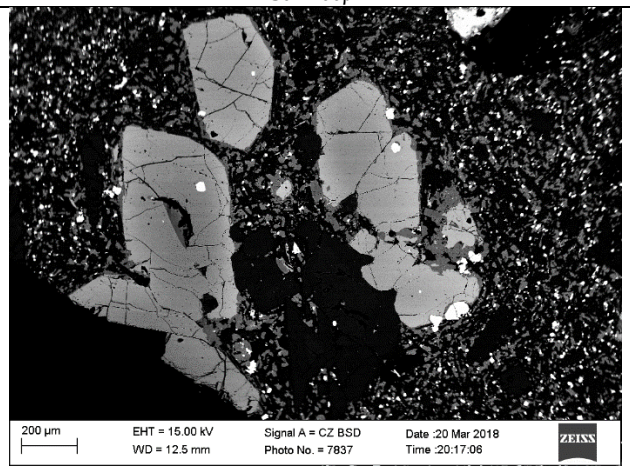	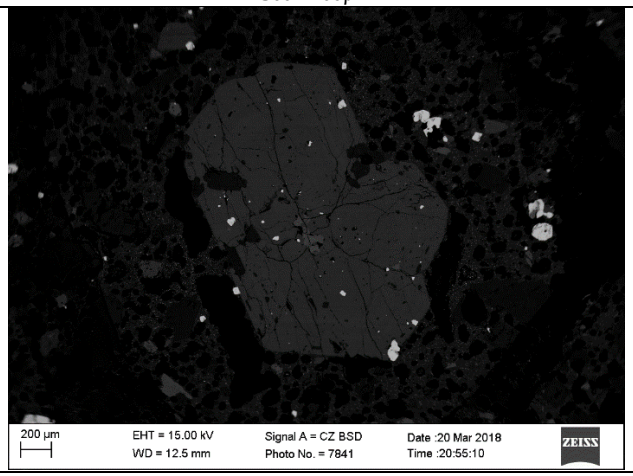	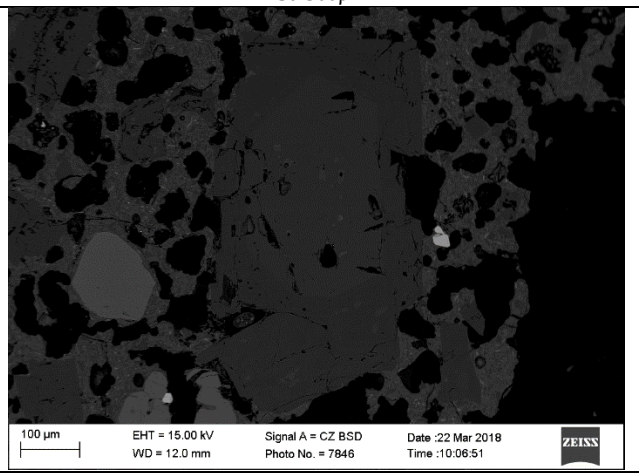

Note each photo scale differs. Descriptions include texture type, comments, zoning patterns, inclusions and Size ranges (>300 µm phenocrysts; 300-100 µm microcrysts; <100 µm microlites). Photomicrographs of each texture taken on a ZEISS Scanning Electron Microscope. Type 1 sample T48; type 2 sample T49; type 3 sample T24.

Table A.3: Main texture descriptions and classification of Orthopyroxene phenocrysts.

Type	1	2
Textural description	Euhedral to subhedral crystals as phenocrysts and subedral to anhedral crystals found as microcrysts. Little chemical variation some crystal fractured and partly weathered. Can be found in clusters with Plag and Cpx.	Euhedral to subhedral single phenocrysts with observed slight chemical variation. Inclusions evident and fractures and weathering sometimes observed. Sometimes observed as microcrysts in clustered groups.
Zonation	No zonation	Concentric zoning comprised of normal and reverse zoning
Inclusions	Melt; titanomagnetite	Melt; titanomagnetite
Size	250-2000µm	500-1100µm
Photo	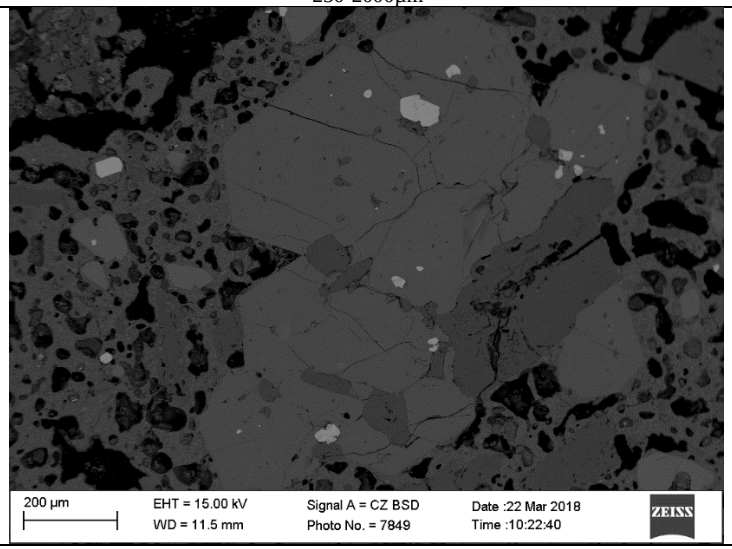	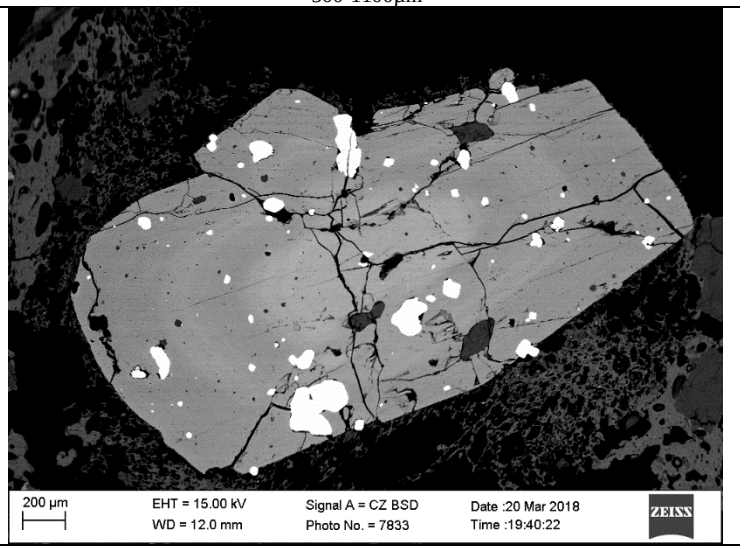

Note each photo scale differs. Descriptions include texture type, comments, zoning patterns, inclusions and Size ranges (>300 µm phenocrysts; 300-100 µm microcrysts; <100 µm microlites). Photomicrographs of each texture taken on a ZEISS Scanning Electron Microscope. Type 1 sample T24; type 2 sample 47.

Table A.4: Main texture descriptions and classification of Olivine phenocrysts.

Type	**1**
Textural description	Euhedral to subhedral phenocrysts observed with anhedral crystals observed as microcrysts. Large phenocrysts sometimes have skeletal shape/texture with fracturing prevalent in all crystals observed. No inclusion seen. No weathering and rarely chemical variation rims observed.
Zonation	No Zonation
Inclusions	No inclusions observed.
Size	100-1000µm
Photo	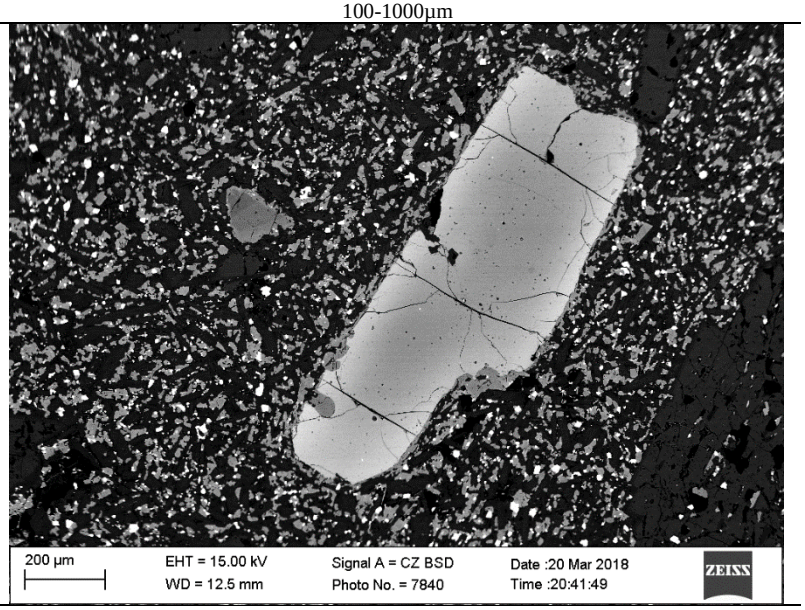

Note each photo scale differs. Descriptions include texture type, comments, zoning patterns, inclusions and Size ranges (>300 µm phenocrysts; 300-100 µm microcrysts; <100 µm microlites). Photomicrographs of each texture taken on a ZEISS Scanning Electron Microscope. Type 1 sample T48.

Table A.5: Main texture descriptions and classification of Amphibole phenocrysts.

Type	**1**
Textural description	Single subhedral to anhedral phenocryst observed with inclusions. Fairly weathered and fractured.
Zonation	Normal zonation
Inclusions	Melt; titanomagnetite
Size	900µm
Photo	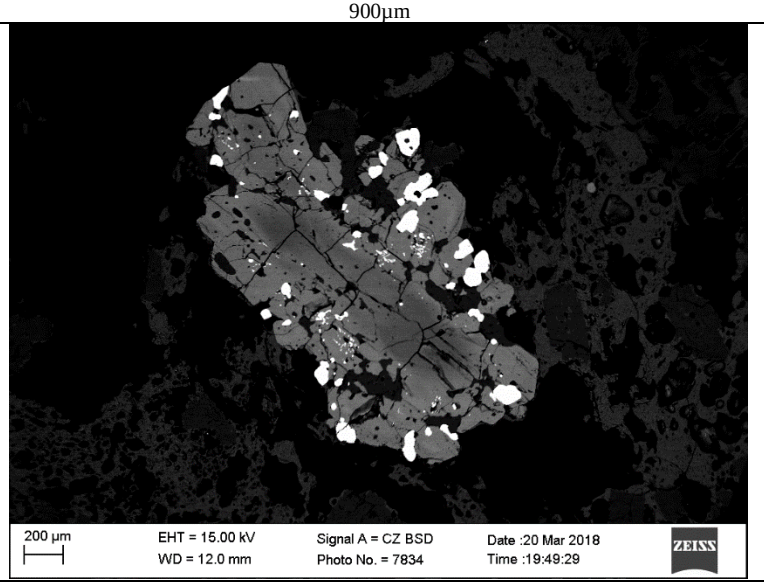

Note each photo scale differs. Descriptions include texture type, comments, zoning patterns, inclusions and Size ranges (>300 µm phenocrysts; 300-100 µm microcrysts; <100 µm microlites). Photomicrographs of each texture taken on a ZEISS Scanning Electron Microscope. Type 1 sample T47.

Background and equations to weathering index; CIA and CIW

Chemical index of alteration (CIA)

The Chemical Index of Alteration, developed by Nesbitt and Young, is the measure of the extent of the conversion of feldspar to clays (Fiantis et. al., 2010). The optimum freshness value is defined as less than 50 while between 50 to 100 would be considered weathered (Fiantis et. al., 2010). It is calculated using molar proportions as below:

$$CIA = \left(\frac{Al_2O_3}{Al_2O_3 + CaO + Na_2O + K_2O}\right) \times 100$$

Chemical index of weathering (CIW)

The Chemical Index of Weathering is the degree of weathering proposed by Harnois (Fiantis et. al., 2010). The index is almost identical to CIA however it eliminates K2O from the equation. The CIW removes the associated K which may yield very high values for K-feldspar rich rocks. Like the CIA, the CIW is essentially the conversion of feldspars to clay minerals such as kaolinite. The optimum freshness observed for CIW is the same as CIA in where less than 50 is considered fresh while above this value is considered weathered (Fiantis et. al., 2010). It is equated using molar proportions as shown below:

$$CIW = \left(\frac{Al_2O_3}{Al_2O_3 + CaO + Na_2O}\right) \times 100$$